

Evolution of Particle Velocity Dispersion in a Circumplanetary Disk Due to Inelastic Collisions and Gravitational Interactions

Keiji Ohtsuki

Computing Service Center, Yamagata University, Yamagata 990-8560, Japan

E-mail: ohtsuki@kj.yamagata-u.ac.jp

Received May 26, 1998; revised September 15, 1998

We study the evolution and equilibrium values of velocity dispersions of particles in a circumplanetary disk, taking into account both inelastic collisions and gravitational interactions between particles. For a disk of particles with a Rayleigh distribution of orbital eccentricities and inclinations, we derive an evolution equation for mean square eccentricities and inclinations on the basis of the Hill's approximations in the three-body problem. We find that the evolution is governed by the terms of viscous stirring and energy equipartition, the latter tending to equalize the product of mass and mean square eccentricities and inclinations of particles with different sizes. Stirring rates of mean square eccentricities and inclinations of nongravitating particles due to direct collisions are obtained analytically. In the case where both direct collisions and gravitational interactions are taken into account, stirring rates are numerically evaluated by three-body orbit integrations, and their Rayleigh distribution averages are calculated. Using these stirring rates, the evolution of the root mean square eccentricities and inclinations of particles are simulated. We confirm that effects of both finite size and gravity of particles play an important role in maintaining nonzero velocity dispersions. For a system with two particle size components, the relative importance of different terms in the evolution equation is investigated and found to vary depending on the relative abundance of particles of each size component. The evolution of root mean square eccentricities and inclinations of particles calculated on the basis of the present formalism is also compared with numerical results of N -body simulations for a disk of particles with low optical depth, and excellent agreement is found between the results of the two methods. © 1999 Academic Press

Key Words: planetary rings; satellites; planetary formation; celestial mechanics; collisional physics.

1. INTRODUCTION

Inelastic collisions and gravitational interactions between constituent particles and satellites are regarded as playing an important role in the dynamics of planetary rings; thus they have been studied in various ways (see, e.g., Nicholson and Dones 1991, Esposito 1993). In earlier studies, effects of inelastic collisions and gravitational interactions were investigated separately: when velocity dispersion evolving through inelastic collisions

was studied, either the effect of gravitational interactions was neglected (e.g., Brahic 1977, Goldreich and Tremaine 1978) or only the overall self-gravity of disk particles in the vertical direction was included (e.g., Araki and Tremaine 1986, Wisdom and Tremaine 1988, Salo 1991, 1992a). On the other hand, in the studies of gravitational interactions between ring particles and a satellite, individual collisions between particles were not considered (e.g., Goldreich and Tremaine 1982, Hénon and Petit 1986, Petit and Hénon 1986).

The simultaneous effects of collisions and gravitational encounters were taken into account in an approximate manner by Lukkari and Salo (1984; see also Salo 1985) in their N -body simulations of planetary rings. In their simulations, the mutual gravitational attraction between particles was included if their distance became smaller than 10 times the particle radius. The results of their simulations demonstrated that the equilibrium velocity dispersion was increased considerably when gravitational encounters were taken into account. Petit and Hénon (1987) fully incorporated both collisions and gravitational interactions between particles into their coplanar three-body orbit integrations and studied changes of orbital elements of particles. They also investigated the equilibrium velocity dispersion by carrying out orbit integrations with various values of initial eccentricities of orbits and restitution coefficient of particles. They found that an equilibrium state with radial excursion of particles of order the particle radii is achieved unless the restitution coefficient is too large. They also studied the distribution of eccentricities of particles, and the results of their orbit integrations suggest that the Rayleigh distribution (see Eq. (12)) of eccentricities seems to be preserved through inelastic collisions and gravitational interactions.

On the other hand, Ohtsuki (1992a, hereafter Paper I) studied the changes of orbits with nonzero inclinations due to collisions and gravitational interactions on the basis of Hill's approximations in the three-body problem. Paper I analytically evaluated change rates of eccentricities and inclinations of ring particles due to inelastic collisions when the relative velocities between particles are large enough to neglect gravitational interactions. It also studied the cases including both collisions and gravitational interactions using three-body orbit integrations. Numerical

results for $e = 2i$ (e and i are eccentricity and inclination of the orbit of particles) and $\varepsilon_n = 1$ (ε_n is the restitution coefficient in the normal direction) showed that effects of gravitational interactions are important for small values of e and i , while they can be neglected when $e \gtrsim 4v_e/v_K$ (v_e is the escape velocity from the particle surface, and v_K is the circular Keplerian velocity of a particle). However, Paper I did not evaluate the stirring rates for the case involving a distribution of eccentricities and inclinations, and particles were assumed to have identical eccentricities and inclinations before encounters. Furthermore, only the case with $\varepsilon_n = 1$ was studied in the orbit integrations.

When both inelastic collisions and gravitational interactions are incorporated, the change of eccentricities and inclinations of particles are determined by the balance between these two effects. Furthermore, if the tidal effect is sufficiently small, gravitational accretion of colliding particles becomes possible. Weidenschilling *et al.* (1984) pointed out that gravitational accretion of particles becomes possible when the sum of the radii of the colliding particles (R_p) is less than their mutual Hill radius (R_H ; see Eqs. (1) and (2)). On the other hand, Ohtsuki (1993) studied the probability of gravitational accretion of colliding particles under the effects of tidal force. Numerical results of three-body orbit integrations showed that accretion is possible but still difficult for $\frac{2}{3} \leq R_p/R_H < 1$, while most sufficiently inelastic collisions lead to accretion when $R_p/R_H < \frac{2}{3}$ and $e \lesssim v_e/v_K$. Assuming random impact orientation, Canup and Esposito (1995) further obtained a simple expression for the criterion of capture which can reproduce the numerical results of Ohtsuki (1993); the derived criterion was used in numerical simulations of reaccretion of disrupted satellites (Canup and Esposito 1995) and lunar accretion (Canup and Esposito 1996, Ida *et al.* 1997).

The above studies in the framework of the three-body problem such as Petit and Hénon (1987) or Paper I can be applied to a particle disk if its optical depth is much less than unity, but they cannot be directly applied to the cases with large optical depth. Recently, dynamics of planetary rings of self-gravitating particles with both low and high optical depths were investigated by Salo (1992b, 1995) and Richardson (1994). These authors utilized the technique of local N -body simulations with periodic boundary conditions, which was first developed by Wisdom and Tremaine (1988) for planetary rings of equal-size particles with the effect of overall self-gravity. Numerical results of Salo (1992b, 1995) and Richardson (1994) confirmed the importance of gravitational interactions in the evolution of velocity dispersion, and in the case of large optical thickness, it was found that gravitational scattering by collective wakes becomes yet more important (Salo 1995). Numerical experiments which correspond to the outer regions of Saturn's rings by Salo (1995) also confirmed formation of particle aggregates by gravitational accretion.

In the present work, we extend our previous analytic and numerical calculations presented in Paper I to cases involving distributions of eccentricities and inclinations of particle orbits, and we also extend our previous three-body orbit integrations to

cases involving inelastic collisions ($\varepsilon_n < 1$). For the orbit integrations with inelastic collisions, only gravitational interactions and rebounds will be investigated; accretion of particles will not be investigated, since this was already discussed previously in Ohtsuki (1993). The results presented here can be applied to the dynamics of planetary rings with low optical depth, such as Saturn's C ring. They should also be helpful to the understanding of fundamental processes related to satellite accretion in a circumplanetary disk with low optical thickness (Stevenson *et al.* 1984, Weidenschilling *et al.* 1984, Ohtsuki 1993, Canup and Esposito 1995, 1996, Ida *et al.* 1997) or theoretical analysis of numerical results of N -body simulations for planetary rings. Moreover, the formulation for the evolution of velocity dispersion derived here (Section 2) can be applied to the disk of planetesimals around the Sun or other astrophysical disks.

In Section 2, an equation is derived for the evolution of the mean square eccentricities and inclinations of particles. Section 3 analytically evaluates the change rates of eccentricities and inclinations of particles due to inelastic collisions in the case where relative velocities between particles are much larger than both $R_p\Omega$ (Ω is the Keplerian angular velocity) and v_e ; under the latter condition, gravitational attraction between particles can be neglected. Cases both with and without a distribution of eccentricities and inclinations are considered. In Section 4, stirring rates are evaluated using three-body orbit integrations with nonzero inclinations, where both inelastic collisions and gravitational interactions are incorporated. Stirring rates averaged over the Rayleigh distribution of particles' eccentricities and inclinations are also obtained. The evolution of root mean square eccentricities and inclinations are simulated using these stirring rates and compared with the numerical results of N -body simulations. Section 5 evaluates equilibrium velocity dispersions in a system of one and two particle size components using the stirring rates obtained by the three-body orbit integrations. Summary of results and discussion are presented in Section 6.

2. FORMULATION FOR THE EVOLUTION OF VELOCITY DISPERSION

As in Paper I, we consider the interaction of particles in Hill's coordinates (Hill 1878, Hénon and Petit 1986, Nakazawa and Ida 1988), where the coordinates of the particles are referred to a reference point that moves on a circular orbit with semimajor axis a_0 at the Keplerian angular velocity $\Omega = \sqrt{GM_c/a_0^3}$ (M_c is the mass of the central body). A rotating Cartesian coordinate system is erected with origin at the reference position, the x axis pointing radially outward, the y axis pointing in the direction of the orbital motion, and the z axis normal to the equatorial plane. The masses of particles are assumed to be much smaller than M_c , and the eccentricity e_j and the inclination i_j of the particles are assumed to be much smaller than unity; in this case, equations for the motion of the particles relative to the reference point can be linearized, and they are written in nondimensional forms if

time is scaled by Ω^{-1} and length by the Hill radius,

$$R_H \equiv h_{12} a_0. \quad (1)$$

Here, h_{12} is defined in terms of M_c and the masses of the mutually interacting particles m_1 and m_2 as

$$h_{12} = \left(\frac{m_1 + m_2}{3M_c} \right)^{1/3}. \quad (2)$$

In the following, tildes are used to denote scaled quantities. The motion of particle j is then expressed as

$$\begin{aligned} \tilde{x}_j &= \tilde{b}_j - \tilde{e}_j \cos(\tilde{t} - \tau_j) \\ \tilde{y}_j &= -\frac{3}{2} \tilde{b}_j (\tilde{t} - \phi_j) + 2\tilde{e}_j \sin(\tilde{t} - \tau_j) \\ \tilde{z}_j &= \tilde{i}_j \sin(\tilde{t} - \omega_j), \end{aligned} \quad (3)$$

where τ_j and ω_j are the time of perihelion passage (scaled by Ω^{-1}) and argument of perihelion, ϕ_j defines the origin of time, and \tilde{e}_j , \tilde{i}_j , and \tilde{b}_j are scaled as

$$\begin{aligned} \tilde{e}_j &= e_j / h_{12} \\ \tilde{i}_j &= i_j / h_{12} \\ \tilde{b}_j &= (a_j - a_0) / h_{12} a_0. \end{aligned} \quad (4)$$

Furthermore, the motions of the two mutually interacting particles can be separated into the relative motion and the center of mass motion, and the center of mass motion is unaffected by collisions or gravitational interactions between particles. The nondimensional equations for the relative motion are written as

$$\begin{aligned} \ddot{\tilde{x}} &= 2\dot{\tilde{y}} + 3\tilde{x} - 3\tilde{x}/\tilde{r}^3 \\ \ddot{\tilde{y}} &= -2\dot{\tilde{x}} - 3\tilde{y}/\tilde{r}^3 \\ \ddot{\tilde{z}} &= -\tilde{z} - 3\tilde{z}/\tilde{r}^3, \end{aligned} \quad (5)$$

where $\tilde{r} = (\tilde{x}^2 + \tilde{y}^2 + \tilde{z}^2)^{1/2}$.

It is also useful to introduce eccentricity and inclination vectors (Hénon and Petit 1986, Nakazawa and Ida 1988) defined by

$$\begin{aligned} \tilde{\mathbf{e}}_j &\equiv (\tilde{e}_j \cos \tau_j, \tilde{e}_j \sin \tau_j) \\ \tilde{\mathbf{i}}_j &\equiv (\tilde{i}_j \cos \omega_j, \tilde{i}_j \sin \omega_j). \end{aligned} \quad (6)$$

Since $\tilde{\mathbf{e}}_j$, $\tilde{\mathbf{i}}_j$, and $\tilde{\mathbf{b}}_j$ are linearly related to \tilde{x}_j , \tilde{y}_j , and \tilde{z}_j (Eq. (3)), excentricity and inclination vectors for the relative and the center of mass motions can be also defined as

$$\begin{aligned} \tilde{\mathbf{e}} &\equiv (\tilde{e} \cos \tau, \tilde{e} \sin \tau) = \tilde{\mathbf{e}}_2 - \tilde{\mathbf{e}}_1 \\ \tilde{\mathbf{i}} &\equiv (\tilde{i} \cos \omega, \tilde{i} \sin \omega) = \tilde{\mathbf{i}}_2 - \tilde{\mathbf{i}}_1 \end{aligned} \quad (7)$$

and

$$\begin{aligned} \tilde{\mathbf{E}} &\equiv (\tilde{E} \cos T, \tilde{E} \sin T) = m'_1 \tilde{\mathbf{e}}_1 + m'_2 \tilde{\mathbf{e}}_2 \\ \tilde{\mathbf{I}} &\equiv (\tilde{I} \cos W, \tilde{I} \sin W) = m'_1 \tilde{\mathbf{i}}_1 + m'_2 \tilde{\mathbf{i}}_2, \end{aligned} \quad (8)$$

where

$$m'_j = \frac{m_j}{m_1 + m_2}. \quad (9)$$

Using these properties, Ida (1990) considered the change rates of eccentricities and inclinations of planetesimals due to gravitational interactions, and his formulation was applied to planetary rings in Paper I. In the present work, the formulation of Ida (1990) is improved by introducing an alternative variable (Eq. (15)), and an equation for the evolution of dispersions of eccentricities and inclinations is obtained.

Here, let us consider the evolution of velocity dispersion of a bimodal population of particles, which consists of two different sizes with mass m_1 and m_2 ; extension to the case with a general size distribution is straightforward, and will be discussed later in this section. Since the center of mass motion is unaffected, the change of \tilde{e}_1^2 of a particle with mass m_1 due to a single encounter with a particle with mass m_2 is given by (Ida 1990)

$$\Delta \tilde{e}_1^2 = m_2^2 \Delta \tilde{e}^2 - 2m'_2 \tilde{\mathbf{E}} \cdot \Delta \tilde{\mathbf{e}}. \quad (10)$$

Then the change rate of the mean square of \tilde{e}_1 due to interactions with component 2 particles is written as

$$\begin{aligned} \frac{d\langle \tilde{e}_1^2 \rangle}{d\tilde{t}} &= \tilde{N}_{s2} \int f(\tilde{e}_1, \tilde{i}_1) f(\tilde{e}_2, \tilde{i}_2) \\ &\times \Delta \tilde{e}_1^2 \frac{3}{2} |\tilde{b}| d\tilde{b} \frac{d\tau_1 d\omega_1}{(2\pi)^2} \frac{d\tau_2 d\omega_2}{(2\pi)^2} d\tilde{e}_1 d\tilde{i}_1 d\tilde{e}_2 d\tilde{i}_2, \end{aligned} \quad (11)$$

where \tilde{N}_{s2} is the surface number density of component 2 particles, $\tilde{b} = \tilde{b}_2 - \tilde{b}_1$ is the difference in the semimajor axes, f is the distribution function of \tilde{e}_j and \tilde{i}_j , and the phase angles τ_1 , ω_1 , τ_2 , and ω_2 are assumed to be uniformly distributed between 0 and 2π .

As for the distribution function $f(\tilde{e}_j, \tilde{i}_j)$, Ida and Makino (1992) carried out N -body simulations of gravitational interactions between planetesimals and found that the distributions of orbital eccentricities and inclinations of planetesimals can be well approximated by a Rayleigh distribution given as

$$f(\tilde{e}_j, \tilde{i}_j) d\tilde{e}_j d\tilde{i}_j = \frac{4\tilde{e}_j \tilde{i}_j}{\langle \tilde{e}_j^2 \rangle \langle \tilde{i}_j^2 \rangle} \exp\left(-\frac{\tilde{e}_j^2}{\langle \tilde{e}_j^2 \rangle} - \frac{\tilde{i}_j^2}{\langle \tilde{i}_j^2 \rangle}\right) d\tilde{e}_j d\tilde{i}_j. \quad (12)$$

This Rayleigh distribution in eccentricity and inclination is equivalent to a triaxial Gaussian distribution of random Cartesian velocities (see, e.g., Lissauer and Stewart 1993, Dones and

Tremaine 1993). For a disk of nongravitating particles orbiting a central gravitating body, numerical simulations by Trulsen (1972) suggested the establishment of the Rayleigh distribution of eccentricities and inclinations due to direct collisions between particles. Petit and Hénon (1987) studied the distribution of eccentricities of ring particles using coplanar three-body orbit integrations, and found that the Rayleigh distribution of eccentricities seems to be preserved through inelastic collisions and gravitational interactions. Recently, Ohtsuki and Emori (in preparation) have carried out local N -body simulations of planetary rings taking both inelastic collisions and gravitational interactions into account. Their numerical results showed that a Rayleigh distribution of eccentricities and inclinations of particles is established as long as the restitution coefficient is sufficiently small ($\varepsilon_n \lesssim 0.6$). Thus, in the present work, the distribution function given by Eq. (12) has also been adopted.

Following Ida (1990), $\tilde{\mathbf{E}}$ and $\Delta\tilde{\mathbf{e}}$ are decomposed into components parallel and normal to $\tilde{\mathbf{e}}$ in order to evaluate the second term of Eq. (10), as

$$\begin{aligned}\tilde{E}_{\parallel} &= \tilde{\mathbf{E}} \cdot \tilde{\mathbf{e}}/\tilde{e} \\ \tilde{E}_{\perp} &= (\tilde{E}^2 - \tilde{E}_{\parallel}^2)^{1/2}\end{aligned}\quad (13)$$

and

$$\begin{aligned}\Delta\tilde{e}_{\parallel} &= \cos\tau \cdot \Delta(\tilde{e}\cos\tau) + \sin\tau \cdot \Delta(\tilde{e}\sin\tau) \\ \Delta\tilde{e}_{\perp} &= \sin\tau \cdot \Delta(\tilde{e}\cos\tau) - \cos\tau \cdot \Delta(\tilde{e}\sin\tau).\end{aligned}\quad (14)$$

Here, instead of $\tilde{\mathbf{E}}$, we introduce an alternative variable $\tilde{\mathbf{E}}^*$ defined by

$$\tilde{\mathbf{E}}^* = \frac{\langle\tilde{e}_2^2\rangle\tilde{\mathbf{e}}_1 + \langle\tilde{e}_1^2\rangle\tilde{\mathbf{e}}_2}{\langle\tilde{e}_1^2\rangle + \langle\tilde{e}_2^2\rangle}, \quad (15)$$

which is related to $\tilde{\mathbf{E}}$ and $\tilde{\mathbf{e}}$ as

$$\tilde{\mathbf{E}}^* = \tilde{\mathbf{E}} - \frac{m'_2\langle\tilde{e}_2^2\rangle - m'_1\langle\tilde{e}_1^2\rangle}{\langle\tilde{e}_1^2\rangle + \langle\tilde{e}_2^2\rangle}\tilde{\mathbf{e}}. \quad (16)$$

We similarly define $\tilde{\mathbf{I}}^*$ instead of $\tilde{\mathbf{I}}$. Corresponding variables were used for relative and center of mass coordinates in a local Cartesian coordinate system by Hornung *et al.* (1985) (see also Stewart and Wetherill 1988) and Brophy *et al.* (1990), but these authors did not use eccentricity or inclination vectors. As in Eq. (8), the components of $\tilde{\mathbf{E}}^*$ and $\tilde{\mathbf{I}}^*$ are expressed as

$$\begin{aligned}\tilde{E}^* &\equiv (\tilde{E}^* \cos T^*, \tilde{E}^* \sin T^*) \\ \tilde{I}^* &\equiv (\tilde{I}^* \cos W^*, \tilde{I}^* \sin W^*).\end{aligned}\quad (17)$$

In terms of $\tilde{\mathbf{E}}^*$ and $\tilde{\mathbf{e}}$, \tilde{E}_{\parallel} and \tilde{E}_{\perp} can be written in simple forms

as

$$\begin{cases} \tilde{E}_{\parallel} = \tilde{E}^* \cos(T^* - \tau) + \frac{m'_2\langle\tilde{e}_2^2\rangle - m'_1\langle\tilde{e}_1^2\rangle}{\langle\tilde{e}_1^2\rangle + \langle\tilde{e}_2^2\rangle}\tilde{e} \\ \tilde{E}_{\perp} = \tilde{E}^* \sin(T^* - \tau). \end{cases} \quad (18)$$

Thus, $\Delta\tilde{e}_1^2$ can be written as

$$\begin{aligned}\Delta\tilde{e}_1^2 &= m_2'^2\Delta\tilde{e}^2 - 2m_2' \left[\tilde{E}^* \cos(T^* - \tau) + \frac{m_2'\langle\tilde{e}_2^2\rangle - m_1'\langle\tilde{e}_1^2\rangle}{\langle\tilde{e}_1^2\rangle + \langle\tilde{e}_2^2\rangle}\tilde{e} \right] \\ &\quad \times \Delta\tilde{e}_{\parallel} + \tilde{E}^* \sin(T^* - \tau)\Delta\tilde{e}_{\perp}.\end{aligned}\quad (19)$$

Furthermore, in order to evaluate the integral of Eq. (11), the variables are changed from $(\tilde{e}_1, \tilde{i}_1, \tau_1, \omega_1, \tilde{e}_2, \tilde{i}_2, \tau_2, \omega_2)$ to $(\tilde{e}, \tilde{i}, \tau, \omega, \tilde{\mathbf{E}}^*, \tilde{\mathbf{I}}^*, T^*, W^*)$. The Jacobian for this transformation is

$$\frac{\partial(\tilde{e}_1, \tilde{i}_1, \tau_1, \omega_1, \tilde{e}_2, \tilde{i}_2, \tau_2, \omega_2)}{\partial(\tilde{e}, \tilde{i}, \tau, \omega, \tilde{\mathbf{E}}^*, \tilde{\mathbf{I}}^*, T^*, W^*)} = \frac{\tilde{e}\tilde{i}\tilde{\mathbf{E}}^*\tilde{\mathbf{I}}^*}{\tilde{e}_1\tilde{i}_1\tilde{e}_2\tilde{i}_2}. \quad (20)$$

Thus, Eq. (11) together with Eq. (12) can be expressed in terms of $\tilde{e}, \tilde{i}, \tilde{\mathbf{E}}^*$, and $\tilde{\mathbf{I}}^*$ as

$$\begin{aligned}\frac{d\langle\tilde{e}_1^2\rangle}{d\tilde{i}} &= \tilde{N}_{s2} \int \frac{16\tilde{e}\tilde{i}\tilde{\mathbf{E}}^*\tilde{\mathbf{I}}^*}{\langle\tilde{e}^2\rangle\langle\tilde{i}^2\rangle\langle\tilde{\mathbf{E}}^{*2}\rangle\langle\tilde{\mathbf{I}}^{*2}\rangle} \\ &\quad \times \exp\left(-\frac{\tilde{e}^2}{\langle\tilde{e}^2\rangle} - \frac{\tilde{i}^2}{\langle\tilde{i}^2\rangle} - \frac{\tilde{\mathbf{E}}^{*2}}{\langle\tilde{\mathbf{E}}^{*2}\rangle} - \frac{\tilde{\mathbf{I}}^{*2}}{\langle\tilde{\mathbf{I}}^{*2}\rangle}\right) \\ &\quad \times \Delta\tilde{e}_1^2 \frac{3}{2} |\tilde{b}| d\tilde{b} \frac{d\tau d\omega dT^* dW^*}{(2\pi)^2} d\tilde{e} d\tilde{i} d\tilde{\mathbf{E}}^* d\tilde{\mathbf{I}}^*,\end{aligned}\quad (21)$$

where $\Delta\tilde{e}_1^2$ is given by Eq. (19). The dispersions appearing in Eq. (21) can be expressed in terms of $\langle\tilde{e}_1^2\rangle$, $\langle\tilde{i}_1^2\rangle$, $\langle\tilde{e}_2^2\rangle$, and $\langle\tilde{i}_2^2\rangle$, as

$$\langle\tilde{e}^2\rangle = \langle\tilde{e}_1^2\rangle + \langle\tilde{e}_2^2\rangle, \quad \langle\tilde{i}^2\rangle = \langle\tilde{i}_1^2\rangle + \langle\tilde{i}_2^2\rangle \quad (22)$$

and

$$\langle\tilde{\mathbf{E}}^{*2}\rangle = \frac{\langle\tilde{e}_1^2\rangle\langle\tilde{e}_2^2\rangle}{\langle\tilde{e}_1^2\rangle + \langle\tilde{e}_2^2\rangle}, \quad \langle\tilde{\mathbf{I}}^{*2}\rangle = \frac{\langle\tilde{i}_1^2\rangle\langle\tilde{i}_2^2\rangle}{\langle\tilde{i}_1^2\rangle + \langle\tilde{i}_2^2\rangle}. \quad (23)$$

In the right-hand side of Eq. (19), $\Delta\tilde{e}^2$, $\Delta\tilde{e}_{\parallel}$, and $\Delta\tilde{e}_{\perp}$ are functions of $\tilde{\mathbf{e}}$ and $\tilde{\mathbf{i}}$ alone. Therefore, integrals over T^* and W^* in Eq. (21) can be evaluated readily, and the terms containing $\tilde{E}^* \cos(T^* - \tau)$ or $\tilde{E}^* \sin(T^* - \tau)$ vanish. Then, integrals over $\tilde{\mathbf{E}}^*$ and $\tilde{\mathbf{I}}^*$ can also be evaluated easily, and we finally obtain

$$\frac{d\langle\tilde{e}_1^2\rangle}{d\tilde{i}} = \tilde{N}_{s2} m_2' \left\{ m_2' \langle P_{\text{VS}} \rangle + \frac{m_2'\langle\tilde{e}_2^2\rangle - m_1'\langle\tilde{e}_1^2\rangle}{\langle\tilde{e}_1^2\rangle + \langle\tilde{e}_2^2\rangle} \langle P_{\text{DF}} \rangle \right\} \quad (24)$$

with

$$\begin{cases} \langle P_{VS} \rangle = \int P_{VS}(\tilde{e}, \tilde{i}) f(\tilde{e}, \tilde{i}) d\tilde{e} d\tilde{i} \\ \langle P_{DF} \rangle = \int P_{DF}(\tilde{e}, \tilde{i}) f(\tilde{e}, \tilde{i}) d\tilde{e} d\tilde{i}, \end{cases} \quad (25)$$

where f is the Rayleigh distribution function (see Eq. (12)) with the dispersions given by Eq. (22), and $P_{VS}(\tilde{e}, \tilde{i})$ and $P_{DF}(\tilde{e}, \tilde{i})$ are the rates of viscous stirring and dynamical friction defined by

$$\begin{cases} P_{VS}(\tilde{e}, \tilde{i}) = \int \Delta \tilde{e}^2 \frac{3}{2} |\tilde{b}| d\tilde{b} \frac{d\tau d\omega}{(2\pi)^2} \\ P_{DF}(\tilde{e}, \tilde{i}) = -2\tilde{e} \int \Delta \tilde{e}_{\parallel} \frac{3}{2} |\tilde{b}| d\tilde{b} \frac{d\tau d\omega}{(2\pi)^2} \end{cases} \quad (26)$$

(Note that the definition of P_{DF} differs from that used in Ida (1990) by a factor of \tilde{e}^2 .) The change rate of $\langle \tilde{i}_1^2 \rangle$ can be expressed in a similar form in terms of viscous stirring and dynamical friction rates for inclinations denoted by $Q_{VS}(\tilde{e}, \tilde{i})$ and $Q_{DF}(\tilde{e}, \tilde{i})$. The change of eccentricity appearing in Eq. (26) ($\Delta \tilde{e}^2$ and $\Delta \tilde{e}_{\parallel}$) is caused by gravitational interactions and/or direct collisions. In the case of nongravitating particles, viscous stirring and energy equipartition arise solely from collisions. Although, by definition, dynamical friction arises from self-gravity, we will use the symbols P_{DF} and Q_{DF} for the terms of energy equipartition even in the case of nongravitating particles.

Recently, Stewart and Ida (1988) independently derived equations for velocity evolution which are essentially identical with the above Eq. (24), and investigated the evolution of orbital eccentricities and inclinations of planetesimals due to gravitational interactions. They derived the velocity evolution equations on the basis of the local-velocity formalism, and also recast them in terms of the Hill orbital elements (such as \tilde{e} or \tilde{i}). In contrast, we used the Hill orbital elements throughout for derivation. In spite of such a difference in derivation, their evolution equation for mean square eccentricity expressed in terms of P_{VS} , P_{DF} , and relative orbital elements is essentially identical with Eq. (24) of this study.

In order to complete the equation for the velocity evolution, the interactions with particles of the same size need to be taken into account. Here, we should recall that the mutual Hill radius $h_{12}a_0$ defined in terms of m_1 and m_2 was used as a unit length in Eq. (24). Thus, Eq. (24) cannot be directly used in this scaled form for the interaction between particles of the same size m_1 . In an unscaled form, Eq. (24) can be expressed as

$$\frac{d\langle e_1^2 \rangle}{dt} = N_{s2} m_2^4 h_{12}^4 a_0^2 \Omega \left\{ m_2' \langle P_{VS} \rangle_{12} + \frac{m_2' \langle e_2^2 \rangle - m_1' \langle e_1^2 \rangle}{\langle e_1^2 \rangle + \langle e_2^2 \rangle} \langle P_{DF} \rangle_{12} \right\} \quad (27)$$

In the above, the suffix “12” has been added to $\langle P_{VS} \rangle$ and $\langle P_{DF} \rangle$, which denotes the interactions between m_1 and m_2 . These stir-

ring rates with the suffix “12” are functions of relative orbital elements scaled by h_{12} defined as Eq. (2). Adding a term for interactions between particles of the same size obtains

$$\frac{d\langle e_1^2 \rangle}{dt} = \sum_{j=1,2} \left[N_{sj} m_j' h_{1j}^4 a_0^2 \Omega \times \left\{ m_j' \langle P_{VS} \rangle_{1j} + \frac{m_j' \langle e_j^2 \rangle - m_1' \langle e_1^2 \rangle}{\langle e_1^2 \rangle + \langle e_j^2 \rangle} \langle P_{DF} \rangle_{1j} \right\} \right], \quad (28)$$

where $m_j' = m_j/(m_1 + m_j)$ and

$$h_{1j} = \left(\frac{m_1 + m_j}{3M_c} \right)^{1/3}. \quad (29)$$

When $j = 1$ on the right-hand side of Eq. (28), the dynamical friction term vanishes and $\langle P_{VS} \rangle_{11}$ denotes the viscous stirring by self-collisions (i.e., interactions between particles of the same size) with $\langle e^2 \rangle = 2\langle e_1^2 \rangle$. Equation (28) can be also applied to a system of more than two size components. If particles have a continuous size distribution, Eq. (28) can be rewritten as

$$\frac{d\langle e_{m_1}^2 \rangle}{dt} = \int n_s(m) m' h_{m_1, m}^4 a_0^2 \Omega \times \left\{ m' \langle P_{VS} \rangle_{m_1, m} + \frac{m' \langle e_m^2 \rangle - m_1' \langle e_{m_1}^2 \rangle}{\langle e_{m_1}^2 \rangle + \langle e_m^2 \rangle} \langle P_{DF} \rangle_{m_1, m} \right\} dm, \quad (30)$$

where $m' = m/(m_1 + m)$, and $n_s(m) dm$ is the surface number density of particles within the mass range of m to $m + dm$.

As an alternative expression, time and length in Eq. (28) may be normalized using Ω^{-1} and $h_0 a_0$, respectively, where h_0 is defined using a certain unit mass m_0 as

$$h_0 = \left(\frac{2m_0}{3M_c} \right)^{1/3}. \quad (31)$$

The unit mass m_0 can be arbitrary; for example, the mass of the largest (or smallest) body in the system may be chosen as m_0 . In this case, Eq. (28) can be written as

$$\frac{d\langle \tilde{e}_1^2 \rangle}{d\tilde{t}} = \sum_{j=1,2} \left[\tilde{N}_{sj} m_j' \tilde{h}_{1j}^4 \times \left\{ m_j' \langle P_{VS} \rangle_{1j} + \frac{m_j' \langle \tilde{e}_j^2 \rangle - m_1' \langle \tilde{e}_1^2 \rangle}{\langle \tilde{e}_1^2 \rangle + \langle \tilde{e}_j^2 \rangle} \langle P_{DF} \rangle_{1j} \right\} \right], \quad (32)$$

where $\tilde{N}_{sj} = N_{sj} (h_0 a_0)^2$ is the number of particles of size component j in the unit area of $(h_0 a_0)^2$, and

$$\tilde{h}_{1j} = h_{1j}/h_0 = \left(\frac{m_1 + m_j}{2m_0} \right)^{1/3}. \quad (33)$$

Equation (30) can also be rewritten in a similar manner as

$$\frac{d\langle \tilde{e}_{m_1}^2 \rangle}{d\tilde{t}} = \int \tilde{n}_s(m) m' \tilde{h}_{m_1, m}^4 \times \left\{ m' \langle P_{VS} \rangle_{m_1, m} + \frac{m' \langle \tilde{e}_{m_1}^2 \rangle - m'_1 \langle \tilde{e}_{m_1}^2 \rangle}{\langle \tilde{e}_{m_1}^2 \rangle + \langle \tilde{e}_m^2 \rangle} \langle P_{DF} \rangle_{m_1, m} \right\} dm. \quad (34)$$

Since masses appear only in the form of mass ratios in Eqs. (32) and (34), the same equations can be applied to different systems as long as the distribution of mass ratios (i.e., distribution of masses normalized by a unit mass defined for each system) is the same.

From Eqs. (28) and (30) (or (32) and (34)), it can readily be seen that the second term in the braces of the right-hand side tends to equalize the mean random kinetic energy of particles with different sizes, i.e., the product of the mass and mean square eccentricities $m_j \langle \tilde{e}_j^2 \rangle$. Since $P_{VS}(\tilde{e}, \tilde{i})$ and $P_{DF}(\tilde{e}, \tilde{i})$ (and also Q_{VS} and Q_{DF}) are functions of orbital elements for relative motion alone, they can be evaluated analytically or by three-body orbit integrations for the relative motion, and then the averaged quantities such as $\langle P_{VS} \rangle$ can be obtained by performing the integration of Eq. (25). Evaluation of these quantities for particles in a circumplanetary disk will be presented in the subsequent sections.

It should be noted that the stirring rates such as $\langle P_{VS} \rangle$ depend on the size of particles in two ways. First, these stirring rates are functions of mean square eccentricities and inclinations of relative motion, which are related to those of each size component as Eq. (22). In general, mean square values such as $\langle \tilde{e}_1^2 \rangle$ or $\langle \tilde{i}_1^2 \rangle$ are functions of particle mass. Thus, the stirring rates such as $\langle P_{VS} \rangle$ take on different values when interactions between different pairs of size components are considered. Second, stirring rates also depend weakly on the mass ratio of the interacting particles as follows. In the nondimensional Hill's equations, the physical size of particles appears in the form of the sum of the radii of colliding particles ($R_{p1} + R_{p2}$) scaled by R_H , which is denoted by \tilde{r}_p as

$$\tilde{r}_p \equiv \frac{R_{p1} + R_{p2}}{R_H} = \left(\frac{9}{4\pi} \right)^{1/3} \rho_p^{-1/3} a_0^{-1} M_c^{1/3} F(\mu), \quad (35)$$

where ρ_p is the material density of a particle, and $F(\mu)$ is a function of the mass ratio $\mu = m_2/m_1$, defined by

$$F(\mu) = \frac{1 + \mu^{1/3}}{(1 + \mu)^{1/3}}. \quad (36)$$

For a given central planet mass M_c and material density ρ_p , \tilde{r}_p is a function of a_0 and the mass ratio μ of the interacting particles. Since we consider interaction within a swarm of particles at a certain local region, the dependence of a_0 does not explicitly appear in the equation for velocity evolution, while the dependence on the mass ratio cannot be neglected; $F(\mu)$ takes its minimum

value of unity when $\mu = 0$ ($m_1 \gg m_2$) and its maximum value of 1.587 when $\mu = 1$ ($m_1 = m_2$). Thus, when the sizes of interacting particles differ, the functional form of the stirring rates changes through its weak dependence on \tilde{r}_p . This dependence is not negligible in the case of the velocity evolution of ring particles where direct collisions play an important role. On the other hand, in the case of interaction between planetesimals orbiting around the sun, $\mathcal{O}(\tilde{r}_p) = 10^{-3}$ to $10^{-4} \ll 1$. In this case, as long as the velocity dispersion is smaller than the escape velocity, gravitational interactions dominate the velocity evolution (e.g., Ohtsuki 1992b, Ohtsuki *et al.* 1993). Thus, the effect of physical impacts as well as the dependence of μ (which determines the physical size of planetesimals) on the stirring rates can be neglected.

Using the formulation described above, we can also derive the mean collision rate between component 1 (with particle mass m_1) and component 2 (with particle mass m_2). We again consider a bimodal population, whose eccentricities and inclinations follow the Rayleigh distribution. Let $\langle \Gamma_{\text{col}} \rangle$ be the average number of collisions experienced between a component-1 particle and a component-2 particle in a unit time interval. Then $\langle \Gamma_{\text{col}} \rangle$ can be expressed as (cf. Eq. (11))

$$\langle \Gamma_{\text{col}} \rangle = \tilde{N}_{s2} \int f(\tilde{e}_1, \tilde{i}_1) f(\tilde{e}_2, \tilde{i}_2) p_{\text{col}} \times \frac{3}{2} |\tilde{b}| d\tilde{b} \frac{d\tau_1 d\omega_1}{(2\pi)^2} \frac{d\tau_2 d\omega_2}{(2\pi)^2} d\tilde{e}_1 d\tilde{i}_1 d\tilde{e}_2 d\tilde{i}_2, \quad (37)$$

where

$$p_{\text{col}} = \begin{cases} 1 & \text{for collision orbits,} \\ 0 & \text{otherwise.} \end{cases} \quad (38)$$

Changing the variables from $(\tilde{e}_1, \tilde{i}_1, \tau_1, \omega_1, \tilde{e}_2, \tilde{i}_2, \tau_2, \omega_2)$ to $(\tilde{e}, \tilde{i}, \tau, \omega, \tilde{E}^*, \tilde{I}^*, T^*, W^*)$, we can express Eq. (37) as (cf. Eq. (21))

$$\langle \Gamma_{\text{col}} \rangle = \tilde{N}_{s2} \int \frac{16\tilde{e}\tilde{i}\tilde{E}^*\tilde{I}^*}{\langle \tilde{e}^2 \rangle \langle \tilde{i}^2 \rangle \langle \tilde{E}^{*2} \rangle \langle \tilde{I}^{*2} \rangle} \times \exp\left(-\frac{\tilde{e}^2}{\langle \tilde{e}^2 \rangle} - \frac{\tilde{i}^2}{\langle \tilde{i}^2 \rangle} - \frac{\tilde{E}^{*2}}{\langle \tilde{E}^{*2} \rangle} - \frac{\tilde{I}^{*2}}{\langle \tilde{I}^{*2} \rangle}\right) \times p_{\text{col}} \frac{3}{2} |\tilde{b}| d\tilde{b} \frac{d\tau d\omega dT^* dW^*}{(2\pi)^2} d\tilde{e} d\tilde{i} d\tilde{E}^* d\tilde{I}^*. \quad (39)$$

In the above, p_{col} is a function of the relative orbital elements alone, since whether a collision occurs or not is determined only by the relative motion. Thus, performing the integration over T^*, W^*, \tilde{E}^* , and \tilde{I}^* , we obtain

$$\langle \Gamma_{\text{col}} \rangle = \tilde{N}_{s2} \langle P_{\text{col}} \rangle \quad (40)$$

with

$$\langle P_{\text{col}} \rangle = \int P_{\text{col}}(\tilde{e}, \tilde{i}) f(\tilde{e}, \tilde{i}) d\tilde{e} d\tilde{i}, \quad (41)$$

where

$$P_{\text{col}}(\tilde{e}, \tilde{i}) = \int p_{\text{col}}(\tilde{e}, \tilde{i}, \tilde{b}, \tau, \omega) \frac{3}{2} |\tilde{b}| d\tilde{b} \frac{d\tau d\omega}{(2\pi)^2} \quad (42)$$

is the collision rate per unit surface number density of particles (Nakazawa *et al.* 1989, Greenzweig and Lissauer 1990). Note that the accretion rate of a planet on a circular orbit in a disk of planetesimals with a Rayleigh distribution of eccentricities and inclinations is given by Eqs. (40) and (41), if we regard $\langle \tilde{e}^2 \rangle$ and $\langle \tilde{i}^2 \rangle$ in Eq. (41) as the mean square eccentricities and inclinations of planetesimals. Thus, the analytic and numerical results obtained by previous work (e.g., Greenzweig and Lissauer 1992, Dones and Tremaine 1993; see also Eq. (55)) for the accretion rate of a planet on a circular orbit in a disk of planetesimals with a Rayleigh distribution of eccentricities and inclinations can be used in the evaluation of the mean collision rate in the case of bimodal size distribution if each size component has a Rayleigh distribution of eccentricities and inclinations.

3. RATES OF NONGRAVITATING PARTICLE STIRRING CAUSED BY INELASTIC COLLISIONS

In the present work, it is assumed that a collision conserves the relative tangential velocity and reduces the absolute value of the relative normal velocity by a factor of ε_n . The change of relative velocity in the local Cartesian coordinates defined in Section 2 is then given by

$$\Delta \dot{\mathbf{x}} = -(1 + \varepsilon_n)(\boldsymbol{\lambda} \cdot \dot{\mathbf{x}})\boldsymbol{\lambda}, \quad (43)$$

where $\dot{\mathbf{x}} = (\dot{x}, \dot{y}, \dot{z})$ is the relative velocity and $\boldsymbol{\lambda} = \tilde{\mathbf{x}}/\tilde{r}_p$ (\tilde{r}_p is defined by Eq. (35)) is a unit vector pointing from the center of particle 1 to the center of particle 2 at the time of impact.

In this section, stirring rates caused by inelastic collisions are studied under the following assumptions: (i) the radial and vertical components of the particles' random velocities are much larger than the escape velocity from the surface of a particle, i.e., $ev_K, iv_K \gg v_e$, where $v_e = \sqrt{2G(m_1 + m_2)/(R_{p1} + R_{p2})}$; (ii) the radial and vertical excursions of particle orbits are much larger than the physical size of the particles, i.e., $ea_0, ia_0 \gg R_p$; (iii) ε_n is constant. In scaled forms, (i) and (ii) can be written as (i) $\tilde{e}, \tilde{i} \gg \tilde{v}_e$ and (ii) $\tilde{e}, \tilde{i} \gg \tilde{r}_p$, where \tilde{v}_e is the scaled escape velocity given by

$$\tilde{v}_e \equiv v_e/R_H\Omega = \sqrt{6/\tilde{r}_p}. \quad (44)$$

With the assumption (i), particle gravity may be neglected. The effects of gravity and the finite size of particles will be discussed in Sections 4 and 5. The case where ε_n is a function of the impact velocity is also considered in Section 5.2.

3.1. Stirring Rates as Functions of \tilde{e} and \tilde{i}

When the scaled eccentricity \tilde{e} and inclination \tilde{i} for relative motion are much larger than \tilde{r}_p , the stirring rates such as $P_{\text{VS}}(\tilde{e}, \tilde{i})$

for nongravitating particles caused by inelastic collisions can be analytically evaluated (Paper I). Appendix A is a summary of the analytic procedures used to obtain these quantities. The results for the three-dimensional ($\tilde{i} \neq 0$) cases are given by

$$\begin{aligned} P_{\text{VS}} &= \frac{2\tilde{r}_p^2(1 + \varepsilon_n)}{\pi} \sqrt{1 + (\tilde{e}/\tilde{i})^2} \left\{ \frac{2\varepsilon_n - 1}{3} E(k) \tilde{e}^2 \right. \\ &\quad \left. - \frac{5(1 + \varepsilon_n)}{16} F(k) \tilde{e}^2 + \frac{5(1 + \varepsilon_n)}{12} E(k) \tilde{i}^2 \right\} \\ Q_{\text{VS}} &= \frac{2\tilde{r}_p^2(1 + \varepsilon_n)}{\pi} \sqrt{1 + (\tilde{e}/\tilde{i})^2} \left\{ \frac{1 + \varepsilon_n}{12} E(k) \tilde{e}^2 \right. \\ &\quad \left. - \frac{1 + \varepsilon_n}{16} F(k) \tilde{e}^2 + \frac{\varepsilon_n - 2}{3} E(k) \tilde{i}^2 \right\} \\ P_{\text{DF}} &= \frac{2\tilde{r}_p^2(1 + \varepsilon_n)}{\pi} E(k) \tilde{e}^2 \sqrt{1 + (\tilde{e}/\tilde{i})^2} \\ Q_{\text{DF}} &= \frac{2\tilde{r}_p^2(1 + \varepsilon_n)}{\pi} E(k) \tilde{i}^2 \sqrt{1 + (\tilde{e}/\tilde{i})^2}. \end{aligned} \quad (45)$$

(Note that the definition of P_{DF} (Q_{DF}) differs by a factor of $2\tilde{e}^2$ ($2\tilde{i}^2$) from that used in Paper I, and errors in the numerical factors of Paper I have been corrected; see Appendix A.) In the above, $E(k)$ is the complete elliptic integral of the second kind with

$$k = \sqrt{3\tilde{e}^2/4(\tilde{e}^2 + \tilde{i}^2)}; \quad (46)$$

$F(k) = \int_0^1 x^2 \sqrt{(1 - k^2 x^2)/(1 - x^2)} dx$ can be expressed in terms of $E(k)$ and $K(k)$, the complete elliptic integral of the first kind, as

$$F(k) = \frac{1}{3k^2} [(2k^2 - 1)E(k) + (1 - k^2)K(k)]. \quad (47)$$

Under the same assumptions made in the derivation of Eqs. (45) (i.e., $\tilde{e}, \tilde{i} \gg \tilde{v}_e, \tilde{r}_p$), the collision rate P_{col} defined by Eq. (42) can also be evaluated analytically and is given by (Nakazawa *et al.* 1989, Greenzweig and Lissauer 1990)

$$P_{\text{col}} = \frac{2\tilde{r}_p^2 E(k)}{\pi} \sqrt{1 + (\tilde{e}/\tilde{i})^2}. \quad (48)$$

Using Eq. (48), P_{DF} and Q_{DF} given in Eqs. (45) are expressed as

$$P_{\text{DF}}/\tilde{e}^2 = Q_{\text{DF}}/\tilde{i}^2 = (1 + \varepsilon_n)P_{\text{col}}, \quad (49)$$

which suggests that the time scale for energy equipartition is of the same order as the collision time under the assumptions adopted here.

P_{VS} and Q_{VS} can also be expressed in the forms

$$P_{VS} = \frac{32E(k)\tilde{e}^2 - 15F(k)\tilde{e}^2 + 20E(k)\tilde{i}^2}{24\pi} \times \tilde{r}_p^2(1 + \varepsilon_n)\sqrt{1 + (\tilde{e}/\tilde{i})^2}\{\varepsilon_n - \varepsilon'_p(\alpha)\} \quad (50)$$

$$Q_{VS} = \frac{4E(k)\tilde{e}^2 - 3F(k)\tilde{e}^2 + 16E(k)\tilde{i}^2}{24\pi} \times \tilde{r}_p^2(1 + \varepsilon_n)\sqrt{1 + (\tilde{e}/\tilde{i})^2}\{\varepsilon_n - \varepsilon'_Q(\alpha)\},$$

where $\alpha = \tilde{i}/\tilde{e}$ and $\varepsilon'_p(\alpha)$ and $\varepsilon'_Q(\alpha)$ are given by

$$\varepsilon'_p(\alpha) = \frac{16E(k) + 15F(k) - 20E(k)\alpha^2}{32E(k) - 15F(k) + 20E(k)\alpha^2} \quad (51)$$

$$\varepsilon'_Q(\alpha) = \frac{3F(k) - 4E(k) + 32E(k)\alpha^2}{4E(k) - 3F(k) + 16E(k)\alpha^2}.$$

From Eqs. (50), it can readily be seen that \tilde{e}^2 increases (decreases) when ε_n is larger (smaller) than $\varepsilon'_p(\alpha)$, while \tilde{i}^2 increases (decreases) when ε_n is larger (smaller) than $\varepsilon'_Q(\alpha)$. For example, $\varepsilon'_p(1/2) = 0.583$, and $\varepsilon'_Q(1/2) = 0.800$. We plot $\varepsilon'_p(\alpha)$ and $\varepsilon'_Q(\alpha)$ in Fig. 1 by the dotted lines.

3.2. Stirring Rates with the Rayleigh Distribution of \tilde{e} and \tilde{i}

Next, we evaluate stirring rates such as $\langle P_{VS} \rangle$ averaged over the Rayleigh distribution of \tilde{e} and \tilde{i} , using Eqs. (12), (25), and

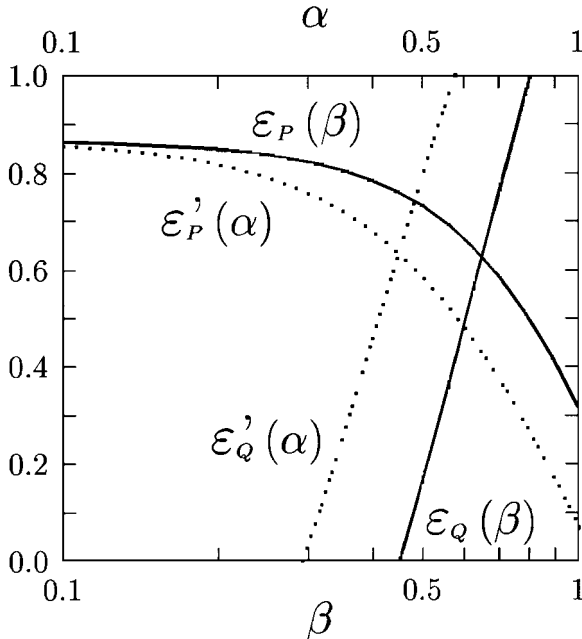


FIG. 1. ε'_p and ε'_Q as functions of $\alpha = \tilde{i}/\tilde{e}$ (dotted lines) and ε_p and ε_Q as functions of β (solid lines).

(45). In the evaluation of the integral in Eq. (25), we adopt the technique used by Greenzweig and Lissauer (1992), who analytically obtained the accretion rate of a protoplanet in a disk of planetesimals with a Rayleigh distribution of eccentricities and inclinations, under the same assumptions adopted here. We outline the calculations in Appendix B. The results for the three-dimensional cases are given by

$$\langle P_{VS} \rangle = \frac{8\tilde{r}_p^2(1 + \varepsilon_n)}{\pi} \langle \tilde{e}^2 \rangle^{1/2} \langle \tilde{i}^2 \rangle^{1/2} \left\{ \frac{2\varepsilon_n - 1}{3} I_e(\beta) - \frac{5(1 + \varepsilon_n)}{16} J_e(\beta) + \frac{5(1 + \varepsilon_n)}{12} I_i(\beta) \right\}$$

$$\langle Q_{VS} \rangle = \frac{8\tilde{r}_p^2(1 + \varepsilon_n)}{\pi} \langle \tilde{e}^2 \rangle^{1/2} \langle \tilde{i}^2 \rangle^{1/2} \left\{ \frac{1 + \varepsilon_n}{12} I_e(\beta) - \frac{1 + \varepsilon_n}{16} J_e(\beta) + \frac{\varepsilon_n - 2}{3} I_i(\beta) \right\} \quad (52)$$

$$\langle P_{DF} \rangle = \frac{8\tilde{r}_p^2(1 + \varepsilon_n)}{\pi} \langle \tilde{e}^2 \rangle^{1/2} \langle \tilde{i}^2 \rangle^{1/2} I_e(\beta)$$

$$\langle Q_{DF} \rangle = \frac{8\tilde{r}_p^2(1 + \varepsilon_n)}{\pi} \langle \tilde{e}^2 \rangle^{1/2} \langle \tilde{i}^2 \rangle^{1/2} I_i(\beta),$$

where

$$\beta \equiv \langle \tilde{i}^2 \rangle^{1/2} / \langle \tilde{e}^2 \rangle^{1/2}, \quad (53)$$

and $I_e(\beta)$, $I_i(\beta)$, and $J_e(\beta)$ are the integrals given below, which can be evaluated numerically (see Fig. 2):

$$I_e(\beta) = \int_0^1 \frac{(1 - \chi^2)E(\frac{\sqrt{3}}{2}\sqrt{1 - \chi^2})}{\{\beta + (\beta^{-1} - \beta)\chi^2\}^3} d\chi,$$

$$I_i(\beta) = \int_0^1 \frac{\chi^2 E(\frac{\sqrt{3}}{2}\sqrt{1 - \chi^2})}{\{\beta + (\beta^{-1} - \beta)\chi^2\}^3} d\chi, \quad (54)$$

$$J_e(\beta) = \int_0^1 \frac{(1 - \chi^2)F(\frac{\sqrt{3}}{2}\sqrt{1 - \chi^2})}{\{\beta + (\beta^{-1} - \beta)\chi^2\}^3} d\chi.$$

The collision rate for a nongravitating protoplanet on a circular orbit averaged over a Rayleigh distribution of planetesimal eccentricities and inclinations was obtained by Greenzweig and Lissauer (1992) and Dones and Tremaine (1993). As mentioned in Section 2, the averaged collision rate derived by these authors is equivalent to $\langle P_{col} \rangle$ defined by Eq. (41), if $\langle \tilde{e}^2 \rangle$ and $\langle \tilde{i}^2 \rangle$ are regarded as the mean square eccentricities and inclinations of particles. In this case, $\langle P_{col} \rangle$ is written as

$$\langle P_{col} \rangle = \frac{4\tilde{r}_p^2}{\pi} I(\beta) \quad (55)$$

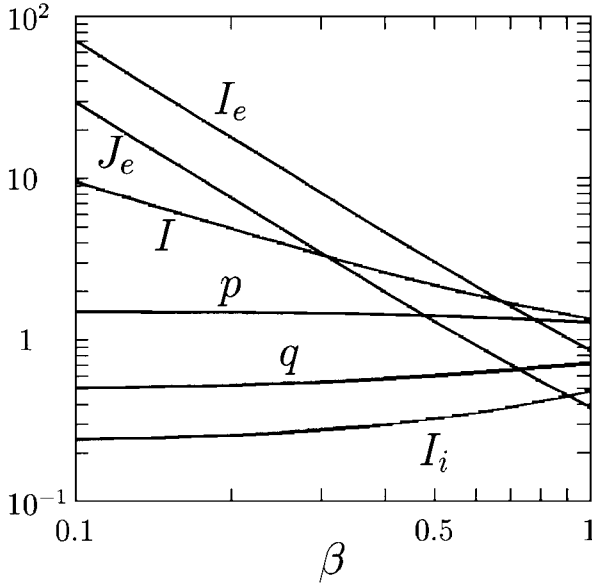


FIG. 2. Numerical values of functions of β ($=\langle \tilde{i}^2 \rangle^{1/2} / \langle \tilde{e}^2 \rangle^{1/2}$). I_e , I_i , and J_e are defined by Eq. (54), I is defined by Eq. (56), and $p = 2\beta I_e / I$ and $q = 2\beta^{-1} I_i / I$ are used in Eq. (57) (see text).

with (see Fig. 2)

$$I(\beta) = \int_0^1 \frac{E\left(\frac{\sqrt{3}}{2}\sqrt{1-\chi^2}\right)}{\{\beta + (\beta^{-1} - \beta)\chi^2\}^2} d\chi. \quad (56)$$

From Eqs. (52) and (55), we find relations similar to Eq. (49) as

$$\begin{aligned} \langle P_{\text{DF}} \rangle / \langle \tilde{e}^2 \rangle &= (1 + \varepsilon_n) p(\beta) \langle P_{\text{col}} \rangle \\ \langle Q_{\text{DF}} \rangle / \langle \tilde{i}^2 \rangle &= (1 + \varepsilon_n) q(\beta) \langle P_{\text{col}} \rangle, \end{aligned} \quad (57)$$

where $p(\beta) = 2\beta I_e(\beta) / I(\beta)$ and $q(\beta) = 2\beta^{-1} I_i(\beta) / I(\beta)$. Both $p(\beta)$ and $q(\beta)$ depend only weakly on β and they take on values of order unity (Fig. 2). Therefore, in the case with the Rayleigh distribution of \tilde{e} and \tilde{i} , it can be also expected that the time scale for energy equipartition due to inelastic collisions between nongravitating particles is of the same order as the collision time.

$\langle P_{\text{VS}} \rangle$ and $\langle Q_{\text{VS}} \rangle$ can be also expressed in the forms

$$\begin{cases} \langle P_{\text{VS}} \rangle = \frac{32I_e(\beta) + 20I_i(\beta) - 15J_e(\beta)}{6\pi} \\ \quad \times \tilde{r}_p^2 (1 + \varepsilon_n) \langle \tilde{e}^2 \rangle^{1/2} \langle \tilde{i}^2 \rangle^{1/2} \{\varepsilon_n - \varepsilon_P(\beta)\} \\ \langle Q_{\text{VS}} \rangle = \frac{4I_e(\beta) + 16I_i(\beta) - 3J_e(\beta)}{6\pi} \\ \quad \times \tilde{r}_p^2 (1 + \varepsilon_n) \langle \tilde{e}^2 \rangle^{1/2} \langle \tilde{i}^2 \rangle^{1/2} \{\varepsilon_n - \varepsilon_Q(\beta)\}, \end{cases} \quad (58)$$

where

$$\begin{aligned} \varepsilon_P(\beta) &= \frac{16I_e(\beta) - 20I_i(\beta) + 15J_e(\beta)}{32I_e(\beta) + 20I_i(\beta) - 15J_e(\beta)} \\ \varepsilon_Q(\beta) &= \frac{32I_i(\beta) - 4I_e(\beta) + 3J_e(\beta)}{4I_e(\beta) + 16I_i(\beta) - 3J_e(\beta)}. \end{aligned} \quad (59)$$

In Fig. 1, we plot $\varepsilon_P(\beta)$ and $\varepsilon_Q(\beta)$ by the solid lines. From Eqs. (58), it can readily be seen that $\langle \tilde{e}^2 \rangle$ increases (decreases) when ε_n is larger (smaller) than $\varepsilon_P(\beta)$, while $\langle \tilde{i}^2 \rangle$ increases (decreases) when ε_n is larger (smaller) than $\varepsilon_Q(\beta)$. If we consider a swarm of particles of the same size, its velocity evolution is determined by viscous stirring alone. In this case, an equilibrium state can be expected only at the crossing point of $\varepsilon_P(\beta)$ and $\varepsilon_Q(\beta)$ in Fig. 1, where $\langle P_{\text{VS}} \rangle = \langle Q_{\text{VS}} \rangle = 0$. We numerically solved these simultaneous equations for ε_n and β , and obtained the critical values

$$\begin{aligned} \varepsilon_{\text{crit}} &= 0.627 \\ \beta_{\text{crit}} &= 0.653. \end{aligned} \quad (60)$$

The above values perfectly coincide with the low-optical-depth limit of the results obtained by Goldreich and Tremaine (1978; see their Figs. 1 and 2— β_{crit} is equivalent to σ_3/σ_1 in their Fig. 2), who solved a Boltzmann equation for nongravitating equal-size ring particles with both low and high optical depths.

4. STIRRING RATES DUE TO COLLISIONS AND GRAVITATIONAL INTERACTIONS

4.1. Stirring Rates without Distributions of \tilde{e} and \tilde{i}

When both direct collisions and gravitational interactions are taken into account, the stirring rates must be evaluated numerically. In this subsection, the case where all the orbits have identical \tilde{e} and \tilde{i} is investigated, since such calculations are helpful to the understanding of the complicated dependence of the stirring rates on parameters such as \tilde{e} , \tilde{i} , and ε_n . We also assume $\tilde{e} = 2\tilde{i}$ in this subsection. We numerically solve the nondimensional Hill's equations for the relative motion of two particles orbiting a planet. Numerical methods for orbital integrations are similar to those used in our previous papers (Paper I, Ohtsuki 1993; see also Ida 1990).

An orbit with a given set of relative orbital elements \tilde{e} , \tilde{i} , \tilde{b} , τ , and ω is integrated in the following manner. When the distance between the particles is large enough to neglect mutual gravity, the solution to the equations of relative motion (Eqs. (5)) can be written as

$$\begin{aligned} \tilde{x} &= \tilde{b} - \tilde{e} \cos(\tilde{t} - \tau) \\ \tilde{y} &= -\frac{3}{2}\tilde{b}(\tilde{t} - \phi) + 2\tilde{e} \sin(\tilde{t} - \tau) \\ \tilde{z} &= \tilde{i} \sin(\tilde{t} - \omega) \end{aligned} \quad (61)$$

and

$$\begin{aligned}\dot{\tilde{x}} &= \tilde{e} \sin(\tilde{t} - \tau) \\ \dot{\tilde{y}} &= -\frac{3}{2}\tilde{b} + 2\tilde{e} \cos(\tilde{t} - \tau) \\ \dot{\tilde{z}} &= \tilde{i} \cos(\tilde{t} - \omega),\end{aligned}\quad (62)$$

where the orbital elements appearing on the right-hand sides of Eqs. (61) and (62) are constant. The azimuthal distance of the guiding center of the epicyclic motion ($\tilde{y}_g \equiv -\frac{3}{2}\tilde{b}(\tilde{t} - \phi)$) at the beginning of integration, \tilde{y}_{g0} , is set to be sufficiently large so that mutual gravity can be neglected (we use $\tilde{y}_{g0} = \max\{100, 20\tilde{e}, 10\tilde{i}\}$). Even if the above value is adopted as \tilde{y}_{g0} , the value of \tilde{b} when $\tilde{y}_g = \tilde{y}_{g0}$ (denoted by \tilde{b}_0) is slightly different from its initial value (denoted by \tilde{b}_∞) at $\tilde{y}_g = \infty$ due to the effect of gravitational attraction between particles, and is approximately expressed as $\tilde{b}_0 \simeq \tilde{b}_\infty - 8/\tilde{y}_{g0}$ (Ida 1990). Thus, initial position and velocity for orbital integration are given by substituting $\tilde{t} = -2\tilde{y}_{g0}/3\tilde{b}_0$, $\tilde{b} = \tilde{b}_0$, and $\phi = 0$ into Eqs. (61) and (62). Under these initial conditions, Eqs. (5) are integrated using eighth-order Runge–Kutta integrator. When a collision between the particles occurs, the velocity change for a given restitution coefficient is calculated according to Eq. (43). The integration is continued until the relative distance becomes large enough again to neglect mutual gravity. After the integration is terminated, $\Delta\tilde{e}^2$, $\Delta\tilde{i}^2$, $\Delta\tilde{e}_\parallel$ and $\Delta\tilde{i}_\parallel$ are calculated for each orbit,

and using these quantities, P_{VS} , Q_{VS} , P_{DF} , and Q_{DF} are evaluated. For noncollision orbits, the stirring rates such as P_{VS} due to gravitational scattering are calculated. We also calculate the stirring rates due to collisions for a given restitution coefficient. The initial orbital elements (\tilde{b} , τ , and ω) of collision orbits for each pair of \tilde{e} and \tilde{i} are recorded and used in other calculations with different values of the restitution coefficient. Thus, only integrations for collision orbits are repeated when the cases with different values of the restitution coefficient are examined.

Figure 3a shows the plots of P_{VS} and Q_{VS} as a function of \tilde{e} when $\varepsilon_n = 1$ and $\tilde{r}_p = 1$; the values of \tilde{e} in units of scaled escape velocity \tilde{v}_e are also indicated on the upper abscissa. In this figure, thick lines with solid circles represent the numerical results of orbit integrations where both collisions and gravitational interactions are taken into account. Thick lines with open circles show the contribution of collisions in the numerical results (thick lines with star symbols will be explained in the next paragraph). The numbers of computed orbits and collision orbits for typical cases in the above calculations are listed in Table I. Finally, thin straight lines in Fig. 3a represent analytic results obtained by Eqs. (45). It can be confirmed that numerical results with mutual gravity coincide with analytic ones when $\tilde{e} \gtrsim 4\tilde{v}_e$ (Paper I). However, numerical values with gravitational effect become substantially larger than the analytic ones when $\tilde{e} \lesssim \tilde{v}_e$. In this low-velocity regime, P_{VS} has almost constant values, since the relative velocity of the particles is

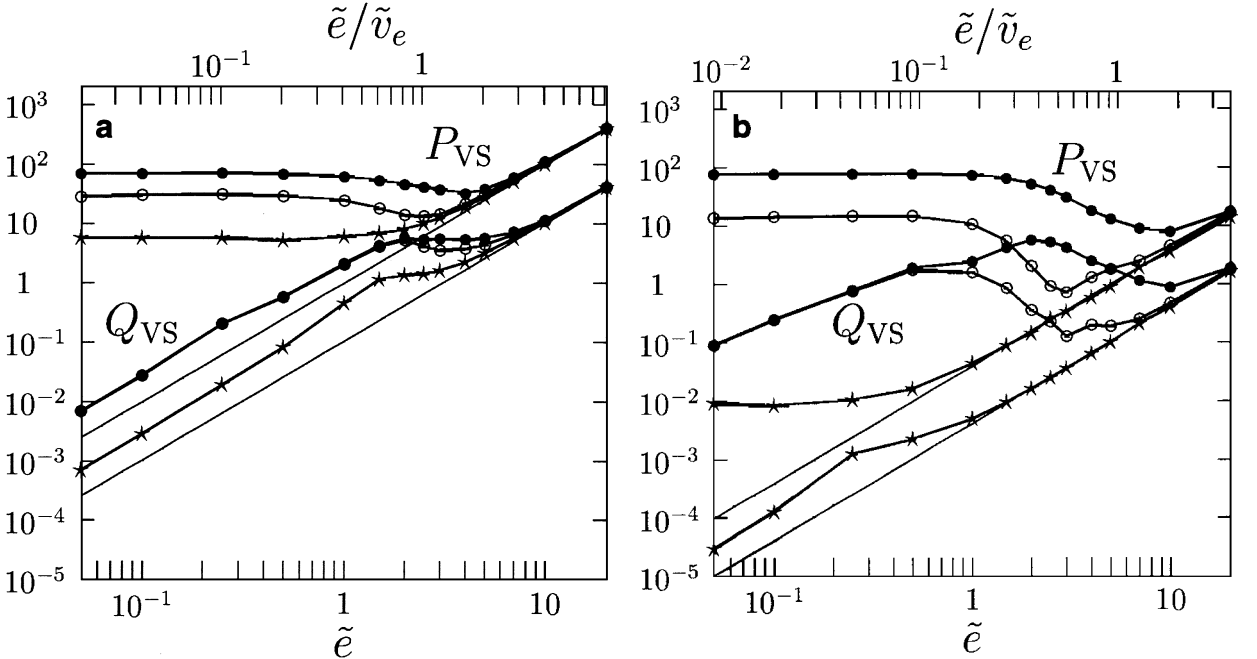


FIG. 3. P_{VS} and Q_{VS} as a function of $\tilde{e} (=2\tilde{i})$ when $\varepsilon_n = 1$ and $\tilde{r}_p = 1$. Values of \tilde{e} in units of the scaled escape velocity \tilde{v}_e are also shown on the upper abscissa. Lines with solid circles show the numerical results with both collisions and gravitational interactions taken into account. Lines with open circles show the contribution of collisions in the above numerical results. Lines with star symbols show the numerical results for nongravitating particles obtained by solving Eq. (63). Thin straight lines represent analytic results calculated by Eq. (45). (b) Same as (a), but with $\tilde{r}_p = 0.2$.

TABLE I
Number of Computed Orbits (N_{comp}) and Collision Orbits (N_{col})
for Typical Cases

$\tilde{e} (=2\tilde{i})$	N_{comp}	N_{col}
0.1	806,400	118,402
1	454,400	47,615
10	1,728,000	19,072

dominated by the Kepler shear, not by the random velocity determined by \tilde{e} and \tilde{i} . When $\tilde{e} \lesssim \tilde{v}_e$, only about 30 to 40% of the total P_{VS} (lines with solid circles) is contributed from collision orbits (lines with open circles), which shows that gravitational scattering is quite important in such a low-velocity regime. For Q_{VS} , on the other hand, the contribution of noncollision orbits is significant only when $2 \lesssim \tilde{e} \lesssim 5$. When $\tilde{e} \gtrsim 5$, gravitational scattering becomes less important due to the high relative velocity. When $\tilde{e} \lesssim 1$, on the other hand, both collisions and gravitational scattering become ineffective in the stirring of inclinations (Paper I, Ida 1990), but collisions are less ineffective. Thus, the effects of noncolliding orbits can be neglected for $\tilde{e} \lesssim 1$ and $\tilde{e} \gtrsim 5$.

The deviation of the numerical results for the three-body orbit integrations from the analytic results can be attributed to effects of mutual gravity and the finite size of particles, both of which have been neglected in the analytic calculations (i.e., we assumed $\tilde{e}, \tilde{i} \gg \tilde{v}_e$ and $\tilde{e}, \tilde{i} \gg \tilde{r}_p$ in Section 3). In order to see these two effects separately, we have carried out orbit integrations neglecting the mutual gravity terms in Eqs. (5). In this case, the

equations for the relative motion are written as

$$\begin{aligned}\ddot{\tilde{x}} &= 2\dot{\tilde{y}} + 3\tilde{x} \\ \ddot{\tilde{y}} &= -2\dot{\tilde{x}} \\ \ddot{\tilde{z}} &= -\tilde{z}.\end{aligned}\tag{63}$$

Numerical results in this nongravitating case with $\varepsilon_n = 1$ and $\tilde{r}_p = 1$ are shown in Fig. 3a by the thick lines with star symbols. We find that the stirring rates at $\tilde{e} \lesssim \tilde{v}_e$ are smaller by about an order of magnitude than the case with mutual gravity. We also find that both P_{VS} and Q_{VS} deviate from the analytic values when $\tilde{e} \lesssim 5\tilde{r}_p$, where the effect of finite size seems to become important. P_{VS} for these nongravitating particles with finite size shows nearly constant values when $\tilde{e} \lesssim \tilde{r}_p$, as in the case with mutual gravity. On the other hand, Q_{VS} in this case shows nearly constant values when $2 \lesssim \tilde{e} \lesssim 3$, but its dependence on \tilde{e} changes when $\tilde{i} \lesssim \tilde{r}_p$ ($\tilde{e} \lesssim 2$). We also investigated this finite size effect by integrating orbits with different \tilde{r}_p . Figure 3b shows the plots of P_{VS} and Q_{VS} when $\tilde{r}_p = 0.2$. We again confirm that numerical results for nongravitating finite size particles deviate from the analytic results when $\tilde{e} \lesssim 5\tilde{r}_p$ ($=1$). P_{VS} for nongravitating finite size particles shows nearly constant values when $\tilde{e} \lesssim \tilde{r}_p$ ($=0.2$), and the dependence of Q_{VS} on \tilde{e} changes when $\tilde{i} \lesssim \tilde{r}_p$ ($=0.2$).

In the case of $\tilde{r}_p = 0.2$, the contribution of collisions to total stirring rates becomes less than for the case of $\tilde{r}_p = 1$; when $\tilde{r}_p = 0.2$ and $\tilde{e} \lesssim 1$, the contribution of noncollision orbits is about 80% of the total P_{VS} , and is as large as 85 to 98% when $1 \lesssim \tilde{e} \lesssim \tilde{v}_e$. Figure 4a shows the change in the contribution of noncollision orbits as a function of \tilde{r}_p . In this figure, $P_{VS, \text{scat}}$ refers to the contribution of noncollision orbits to P_{VS} , and the

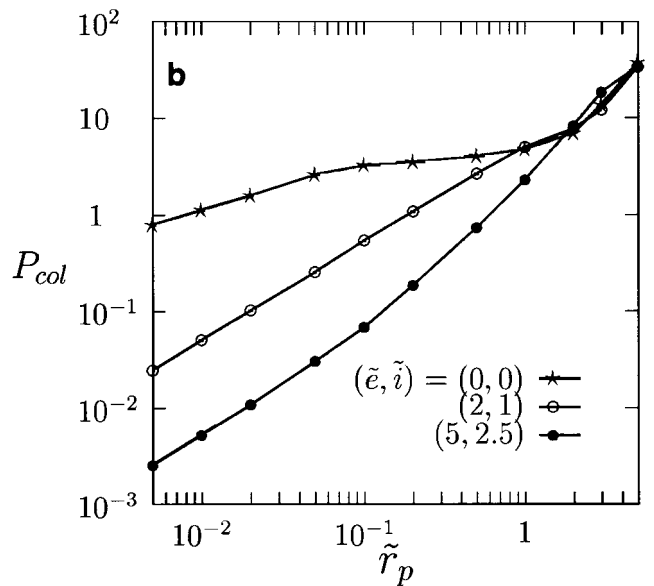
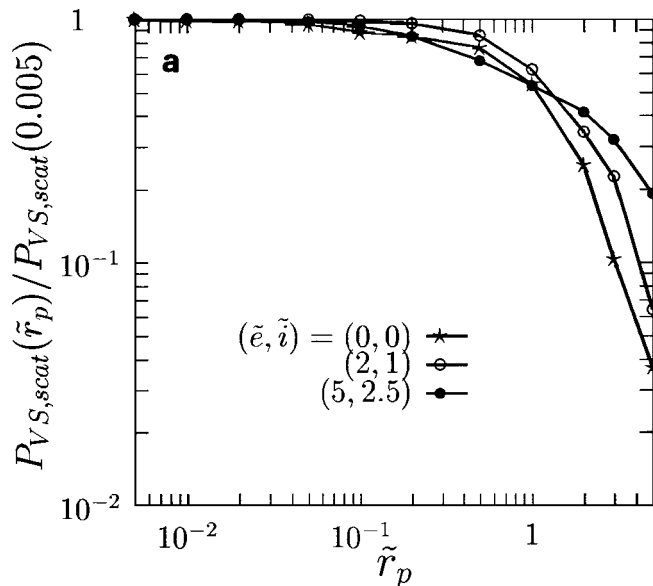


FIG. 4. (a) Stirring rates due to noncollision orbits, as a function of \tilde{r}_p ; ordinate values are expressed relative to the case of $\tilde{r}_p = 0.005$. Values for three different pairs of (\tilde{e}, \tilde{i}) are shown. (b) Nondimensional collision rate as a function of \tilde{r}_p .

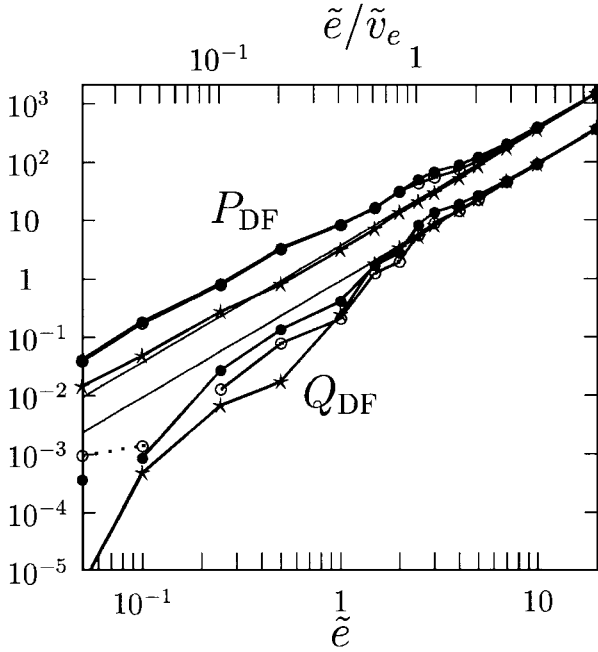


FIG. 5. P_{DF} and Q_{DF} as a function of \tilde{e} ($=2\tilde{i}$) when $\varepsilon_n = 1$ and $\tilde{r}_p = 1$. Negative values of Q_{DF} for $\tilde{e} \lesssim 10^{-1}$ are shown by the dotted line. When Q_{DF} changes its sign, its data points are not connected. Thin straight lines represent analytic results calculated by Eq. (45).

values are expressed relative to the case of $\tilde{r}_p = 0.005$ (this value of \tilde{r}_p corresponds to planetesimals of $\rho_p = 3 \text{ g cm}^{-3}$ orbiting the Sun at $a_0 = 1 \text{ AU}$). The nondimensional collision rates (Eq. (42)) for these cases are shown in Fig. 4b. It is confirmed in Fig. 4a that the contribution of noncollision orbits decreases as \tilde{r}_p (thus the collision rate) increases. It is found that $P_{\text{VS}, \text{scat}}$ can be well approximated by the value with $\tilde{r}_p = 0.005$ when $\tilde{r}_p \lesssim 0.1$. However, the contribution of noncollision orbits is reduced by 15 to 33% when $\tilde{r}_p = 0.5$, and it becomes substantially smaller when $\tilde{r}_p \gtrsim 1$. Thus, both collisions and gravitational scattering are important when $\tilde{r}_p \gtrsim 0.5$, while gravitational scattering dominates velocity evolution when $\tilde{r}_p \lesssim 0.1$, unless the random velocity of the particles is too large.

Figure 5 shows the plots of P_{DF} and Q_{DF} when $\varepsilon_n = 1$ and $\tilde{r}_p = 1$. In this case, the difference between numerical results with mutual gravity and analytic values is not so large as in the cases of P_{VS} and Q_{VS} . These positive values of P_{DF} and Q_{DF} ensure that the terms containing $\langle P_{\text{DF}} \rangle$ and $\langle Q_{\text{DF}} \rangle$ in the evolution equation (e.g., Eq. (24)) tend to equalize random kinetic energy. It is confirmed that numerical results with mutual gravity coincide with analytic values when $\tilde{e} \gtrsim 4\tilde{v}_e$. When $\tilde{i} \lesssim \tilde{r}_p$, the fluctuation in the values of Q_{DF} becomes relatively large (especially when the number of collision orbits found by orbit integrations for a given pair of \tilde{e} and \tilde{i} was not sufficiently large), probably owing to the finite number of collision orbits found by orbit integrations; even negative values are occasionally observed when $\tilde{e} \lesssim 0.1$ (shown by the disconnected points or the dotted line in Fig. 5). However, in such a low-velocity regime, $|Q_{\text{DF}}| (\lesssim 10^{-3})$

is much smaller than $|Q_{\text{VS}}|$ ($\sim 10^{-2}$; see Fig. 3a); thus the effect of such irregular behavior of Q_{DF} on the velocity evolution can be neglected.

So far, we have shown only the cases of elastic collisions ($\varepsilon_n = 1$). Figure 6 shows the plots of P_{VS} and Q_{VS} for cases of inelastic collisions. When these stirring rates have negative values, their absolute values are plotted by dotted lines. According to the analytic results given by Eqs. (50) and (51), in the case of the high velocity limit with $\tilde{e} = 2\tilde{i}$, P_{VS} becomes negative when $\varepsilon_n < \varepsilon'_Q(1/2) (=0.583)$ and Q_{VS} becomes negative when $\varepsilon_n < \varepsilon'_Q(1/2) (=0.800)$. Since $\varepsilon'_p(1/2) < \varepsilon_n (=0.7) < \varepsilon'_Q(1/2)$ in the case of Fig. 6a, the analytic values of P_{VS} are always positive (shown by the thin solid line), while those for Q_{VS} are always negative (shown by the thin dashed line). When the effects of mutual gravity and finite size of particles are taken into account, however, both P_{VS} and Q_{VS} show positive values in the low velocity regime. In the case with mutual gravity, Q_{VS} changes its sign at $\tilde{e} \simeq 5.4$. When \tilde{e} is smaller than this critical value, stirring due to the effects of mutual gravity and finite size overcomes the inelastic dissipation; thus inclinations are enhanced. On the other hand, Q_{VS} in the case of nongravitating particles with finite size changes its sign at a slightly smaller value of \tilde{e} ; in this case, Q_{VS} takes on positive values in the low velocity regime due to finite size effects alone. Figures 6b and 6c show the cases of $\varepsilon_n = 0.5$ and 0.1 , respectively. In these cases, both P_{VS} and Q_{VS} are negative in the high velocity limit. On the other hand, in the low velocity regime where the effects of mutual gravity and finite size are important ($\tilde{e} \lesssim 1$), these quantities show positive values; P_{VS} changes its sign at $\tilde{e} \simeq 4.0$ when $\varepsilon_n = 0.5$ and at $\tilde{e} \simeq 3.6$ when $\varepsilon_n = 0.1$, while Q_{VS} changes its sign at $\tilde{e} \simeq 3.7$ when $\varepsilon_n = 0.5$ and at $\tilde{e} \simeq 3.1$ when $\varepsilon_n = 0.1$. In both cases of $\varepsilon_n = 0.5$ and 0.1 , P_{VS} and Q_{VS} change their sign at $1 \lesssim \tilde{e}/\tilde{v}_e \lesssim 2$. These results reflect the fact that the effects of gravitational scattering and the finite size of particles are strong enough to enhance \tilde{e} and \tilde{i} when $\tilde{e} \lesssim \tilde{v}_e$ or $\tilde{e} \lesssim \tilde{r}_p$, while inelastic collisions become dominant at larger values of \tilde{e} , which tend to decrease \tilde{e} and \tilde{i} as long as $\varepsilon_n < \varepsilon'_p$ and $\varepsilon_n < \varepsilon'_Q$. Therefore, as long as $\varepsilon_n < \varepsilon'_p$ and $\varepsilon_n < \varepsilon'_Q$, critical values at which P_{VS} or Q_{VS} change their sign do not depend on ε_n significantly. Figures 6a and 6b show that the critical value is given by $\tilde{e} \simeq \tilde{i} \simeq \tilde{v}_e$ (i.e., $e \simeq i \simeq v_e/v_K$) in the case with mutual gravity, while it is given by $\tilde{e} \simeq \tilde{i} \simeq \tilde{r}_p$ (i.e., $e \simeq i \simeq R_p \Omega/v_K$) for nongravitating particles with finite size (Brahic 1977, Salo 1995).

We also obtained P_{DF} and Q_{DF} for inelastic cases. We find that their behavior does not significantly depend on ε_n , and is quite similar to the case of $\varepsilon_n = 1$ (Fig. 7). Therefore, the tendency to energy equipartition can be expected also in inelastic cases, as long as P_{DF} and Q_{DF} are comparable to or larger than P_{VS} and Q_{VS} .

4.2. Stirring Rates with Rayleigh Distributions of \tilde{e} and \tilde{i}

Next, we evaluate the stirring rates for gravitating particles when their eccentricities and inclinations have the Rayleigh distribution given as Eq. (12). In this case, the averages of stirring

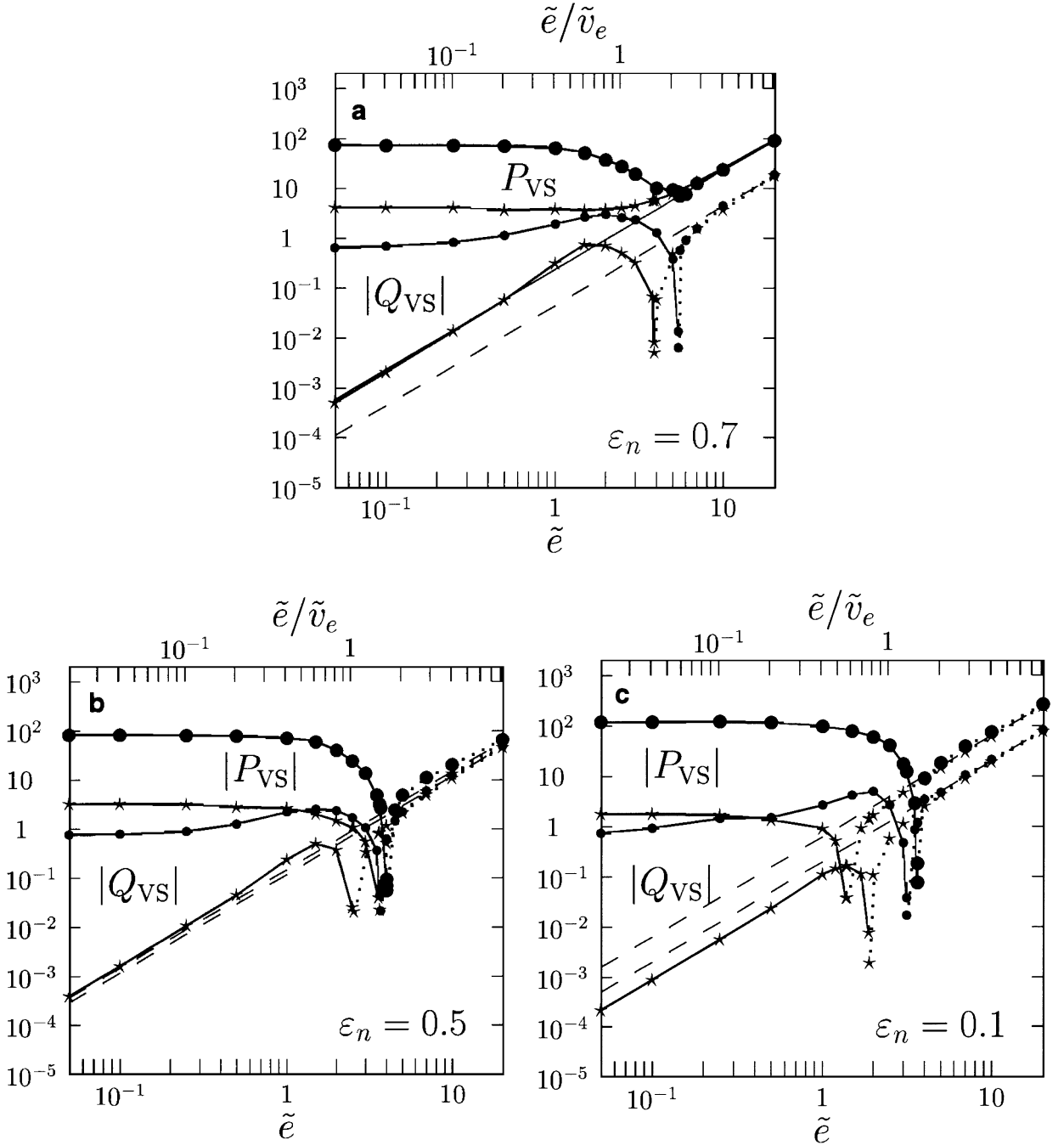


FIG. 6. P_{VS} and Q_{VS} for cases of inelastic collisions ($\tilde{\epsilon} = 2\tilde{i}$ and $\tilde{r}_p = 1$). When they have negative values, their absolute values are plotted by dotted lines. Lines with solid circles and star symbols show the numerical results for gravitating and nongravitating particles with finite size, respectively. Thin straight lines represent analytic results calculated by Eq. (45); a solid line (P_{VS} for $\varepsilon_n = 0.7$) represents positive values, and dashed lines represent negative values. Three cases with $\varepsilon_n = 0.7, 0.5$, and 0.1 are shown.

rates (such as P_{VS}) over the distribution function (see Eq. (25)) are calculated in the following manner. First, we carry out the three-body orbit integrations for a hundred pairs of $\tilde{\epsilon}$ and \tilde{i} defined by

$$(\tilde{\epsilon}, \tilde{i}) = (10^{(m-5)/4}, 10^{(n-5)/4}) \quad (m, n = 1, 2, \dots, 10). \quad (64)$$

The numerical methods for the orbit integrations are the same as described in Section 4.1. Next, we extrapolate the stirring rates obtained for the above 100 points on the $\tilde{\epsilon} - \tilde{i}$ plane to the range of $10^{-3} \leq \tilde{\epsilon}$ (or \tilde{i}) $< 10^{-1}$ and $10^{5/4} < \tilde{\epsilon}$ (or \tilde{i}) $\leq 10^2$. As we can confirm in the numerical results presented in Section 4.1, the values of the stirring rates in most cases can

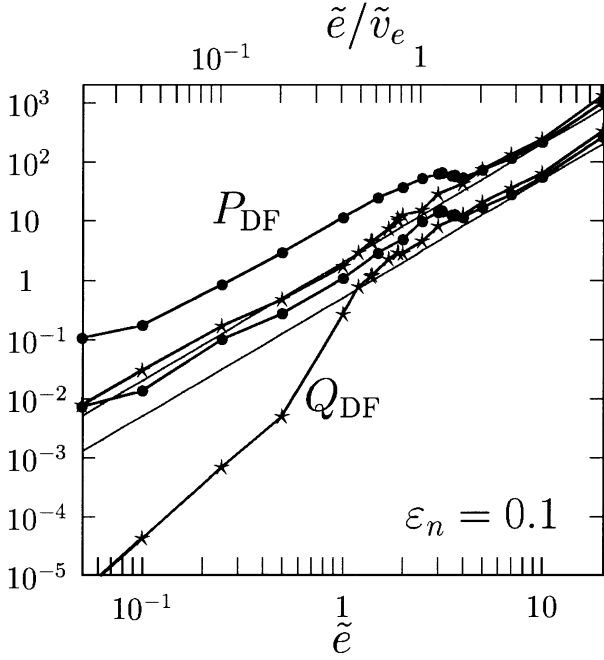


FIG. 7. P_{DF} and Q_{DF} in the case of $\varepsilon_n = 0.1$ ($\tilde{e} = 2\tilde{i}$ and $\tilde{r}_p = 1$). Numerical results for gravitating (lines with solid circles) and nongravitating (lines with star symbols) particles, and analytic results (straight lines) are shown.

be well approximated by a power law with respect to \tilde{e} and \tilde{i} in the low and high velocity limits. As we have mentioned in Section 4.1, fluctuations were found in the numerical values of P_{DF} when $\tilde{e} \sim 10^{-1}$ and $\tilde{i} > 1$, and those of Q_{DF} when $\tilde{e} \sim 10^{-1}$ and $\tilde{i} < 1$. In these cases, we extrapolate the unfluctuating numerical values which were obtained with better accuracy (e.g., P_{DF} at $\tilde{e} \gtrsim 1$). Fortunately, absolute values of P_{DF} and Q_{DF} in such low \tilde{e} cases are small ($< 10^{-1}$) compared with the values with larger \tilde{e} 's. Thus, the values of averaged stirring rates ($\langle P_{\text{DF}} \rangle$ or $\langle Q_{\text{DF}} \rangle$) do not depend sensitively on the manner of extrapolation in such low \tilde{e} cases. By the extrapolation of the numerical results obtained by orbit integrations, we obtain the stirring rates defined at 441 points (including the 100 points defined by Eq. (64)) on the $\tilde{e} - \tilde{i}$ plane, where the values of \tilde{e} and \tilde{i} at each point are given as

$$(\tilde{e}, \tilde{i}) = (10^{(m-13)/4}, 10^{(n-13)/4}) \quad (m, n = 1, 2, \dots, 21). \quad (65)$$

Using these data, we perform the integral given as Eq. (25) and evaluate the collision and stirring rates averaged over the Rayleigh distributions of \tilde{e} and \tilde{i} . The validity of the above numerical procedure to obtain the Rayleigh distribution averages has been confirmed using the analytic collision and stirring rates with and without the Rayleigh distribution described in Section 3. We have calculated the collision and stirring rates in the case of $\tilde{r}_p = 1$ and $\varepsilon_n = 1$ for the above 441 points on the $\tilde{e} - \tilde{i}$ plane by Eq. (45), and the Rayleigh distribution averages of these rates were calculated using these 441 values with given values

of $\langle \tilde{e}^2 \rangle^{1/2}$ and $\langle \tilde{i}^2 \rangle^{1/2}$ (we have examined the case with $\langle \tilde{e}^2 \rangle^{1/2} = 2\langle \tilde{i}^2 \rangle^{1/2}$). We have found that the averaged rates such as $\langle P_{\text{VS}} \rangle$ obtained by the above procedure agree with those given by Eq. (52) within 4%, as long as $10^{-1} \lesssim \langle \tilde{e}^2 \rangle^{1/2} (= 2\langle \tilde{i}^2 \rangle^{1/2}) \lesssim 60$.

Figure 8 shows the plots of nondimensional collision rates with and without the distribution of eccentricities and inclinations. The line with solid circles shows P_{col} defined as Eq. (42), which was obtained by the three-body orbit integrations (solid circles represent the points at which orbit integrations have been carried out); the values in the case of $\tilde{e} = 2\tilde{i}$ and $\tilde{r}_p = 1$ are plotted as a function of \tilde{e} . The dashed line shows the analytic values of the collision rates for gravitating particles ($P_{\text{col,ana}}$) in the case of $\tilde{e} = 2\tilde{i}$, which were calculated from the following expression obtained by Greenzweig and Lissauer (1990):

$$P_{\text{col,ana}} = \frac{2\tilde{r}_p^2 E(k)}{\pi} \sqrt{1 + (\tilde{e}/\tilde{i})^2} \left\{ 1 + \frac{\tilde{v}_e^2}{\tilde{e}^2 + \tilde{i}^2} \frac{K(k)}{E(k)} \right\}. \quad (66)$$

Note that Eq. (66) is reduced to Eq. (48) when $\tilde{e}^2 + \tilde{i}^2 \gg \tilde{v}_e^2$. It can be found that P_{col} agrees with the analytic values when $\tilde{e} \gtrsim 4\tilde{v}_e$, and it can be well approximated by $P_{\text{col,ana}}$ as long as $\tilde{e} \gtrsim \tilde{v}_e$. However, in the low eccentricity region with $\tilde{e} \lesssim 2$ ($\simeq 0.8\tilde{v}_e$) where Kepler shear dominates the relative velocity between particles, P_{col} deviates from $P_{\text{col,ana}}$ and takes on nearly constant values. $\langle P_{\text{col}} \rangle$ in the case of $\langle \tilde{e}^2 \rangle^{1/2} = 2\langle \tilde{i}^2 \rangle^{1/2}$ obtained

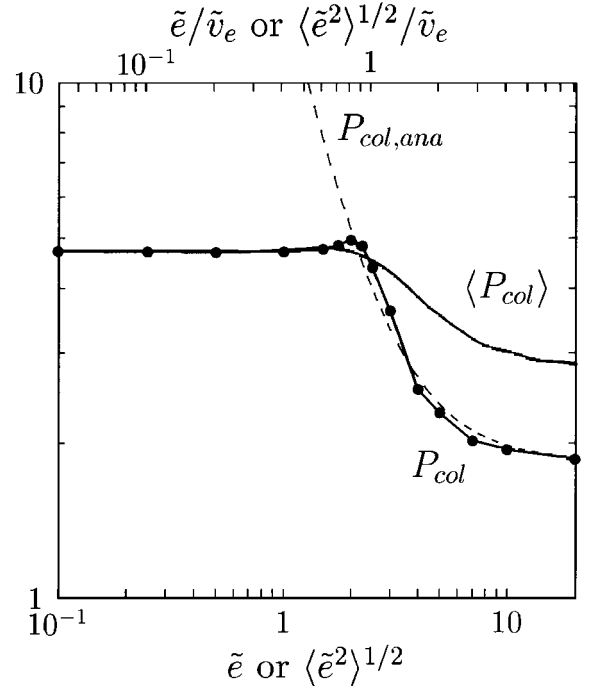


FIG. 8. Nondimensional collision rates P_{col} (obtained by orbit integrations) and $P_{\text{col,ana}}$ (calculated by Eq. (66)) in the case of $\tilde{e} = 2\tilde{i}$ and $\tilde{r}_p = 1$ as a function of \tilde{e} , and $\langle P_{\text{col}} \rangle$ (the Rayleigh distribution average of P_{col}) in the case of $\langle \tilde{e}^2 \rangle^{1/2} = 2\langle \tilde{i}^2 \rangle^{1/2}$ as a function of $\langle \tilde{e}^2 \rangle^{1/2}$.

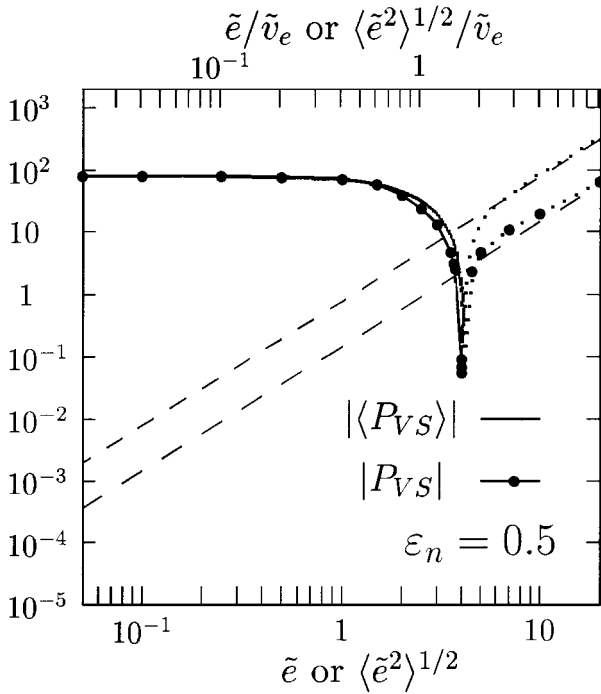


FIG. 9. Nonaveraged stirring rate P_{VS} as a function of \tilde{e} ($=2\tilde{i}$) and the Rayleigh distribution average $\langle P_{VS} \rangle$ as a function of $\langle \tilde{e}^2 \rangle^{1/2}$ ($=2\langle \tilde{i}^2 \rangle^{1/2}$). Absolute values of these rates are plotted, and the dotted lines represent negative values. Analytic values of P_{VS} and $\langle P_{VS} \rangle$ calculated by Eqs. (45) and (52) are also shown by the dashed lines.

from the average of 441 numerical data is plotted as a function of $\langle \tilde{e}^2 \rangle^{1/2}$ with the solid line without symbols. It can be seen that $\langle P_{col} \rangle$ for a given value of $\langle \tilde{e}^2 \rangle^{1/2}$ is larger than P_{col} at $\tilde{e} = \langle \tilde{e}^2 \rangle^{1/2}$ when $\tilde{e} \gtrsim \tilde{v}_e$, since the enhanced collision rates of low \tilde{e} particles overcompensate for the diminished rates of high \tilde{e} particles. A similar tendency was found by Ohtsuki and Ida (1990) and Greenzweig and Lissauer (1992), who calculated the Rayleigh distribution average of planetary accretion rates.

As an example of the stirring rate, we show in Fig. 9 the plots of P_{VS} with and without the distribution of \tilde{e} and \tilde{i} ($\epsilon_n = 0.5$ and $\tilde{r}_p = 1$). The solid and dotted lines with solid circles show the numerical results of the three-body orbit integrations with $\tilde{e} = 2\tilde{i}$, and the lines without symbols show the Rayleigh distribution average of P_{VS} . In both cases, solid parts of the lines show positive values of the stirring rates, while dotted parts show negative values. Analytic values of P_{VS} and $\langle P_{VS} \rangle$ calculated respectively by Eqs. (45) and (52) are also shown by the dashed lines. Note that analytic values are always negative in this case, and their absolute values change as $|P_{VS}| \propto \tilde{e}^2$ or $|\langle P_{VS} \rangle| \propto \langle \tilde{e}^2 \rangle$. It is found that both P_{VS} and $\langle P_{VS} \rangle$ can be well approximated by the analytic values when \tilde{e} or $\langle \tilde{e}^2 \rangle^{1/2}$ is comparable to or larger than $3\tilde{v}_e$. As in the case of P_{col} , P_{VS} takes on nearly constant values when $\tilde{e} \lesssim 1$. Thus, the values of $\langle P_{VS} \rangle$ in such low $\langle \tilde{e}^2 \rangle^{1/2}$ regions are also nearly constant and equal to those of the unaveraged P_{VS} . On the other hand, $|\langle P_{VS} \rangle|$ for a given value of

$\langle \tilde{e}^2 \rangle^{1/2}$ is larger than $|P_{VS}|$ at $\tilde{e} = \langle \tilde{e}^2 \rangle^{1/2}$ when $\tilde{e} \gtrsim 2\tilde{v}_e$, owing to the contribution of the enhanced negative stirring rates of high \tilde{e} particles.

4.3. Evolution of Velocity Dispersions: Comparison with N -Body Simulations

Once the stirring rates averaged over the Rayleigh distribution of eccentricities and inclinations are obtained as described in Section 4.2, the evolution of mean square eccentricities and inclinations of particles in a disk of low optical depth can be studied by Eq. (28) or (30) (or Eq. (32) or (34)). In order to examine the validity of these evolution equations described in Section 2 and the averaged stirring rates obtained by the procedure described in Section 4.2, we have performed comparisons with N -body simulations. We calculated the evolution of dispersions of eccentricities and inclinations of particles using Eq. (32) together with the averaged stirring rates obtained in the manner described in Section 4.2. We also carried out local N -body simulations with periodic boundary conditions taking both inelastic collisions and gravitational interactions into account, and compared the numerical results with the above evolution of dispersions. Our numerical method is similar to that of Salo (1992b, 1995), and will be presented in a separate paper together with detailed numerical results.

Here, two examples of our comparisons are shown in Figs. 10a and 10b. In these figures, the numerical results of our N -body simulations are shown by the solid lines, and those obtained from Eq. (32) with the averaged three-body stirring rates are shown by the dashed lines. Figure 10a shows the case where all the particles have identical sizes ($\tilde{r}_p = 1$); since the nondimensional equations of motion based on Hill's formalism are also solved in our N -body simulation, the mass of a particle does not need to be specified. The values of root-mean-squared eccentricities and inclinations shown in this figure are normalized by Eq. (31), where m_0 in this case was chosen to be the mass of the particle. The surface number density of particles is expressed in terms of the dynamical optical depth (Wisdom and Tremaine 1988), defined by

$$\tau = N\pi R_p^2/S, \quad (67)$$

where R_p is the radius of a particle, S is the area of the simulation cell, and N is the number of particles in the cell ($N = 255$). The case of two size components with $m_L/m_S = 8$ (m_L and m_S are the mass of a large and a small particle, respectively), $N_L = 210$ and $N_S = 840$ is shown in Fig. 10b. In this case, the mass of the larger particle (m_L) was chosen as the unit mass used in Eq. (31). The optical depths for large and small particles are denoted by τ_L and τ_S , respectively. In both Figs. 10a and 10b, ϵ_n is equal to 0.5.

These two figures allow us to confirm excellent agreement between N -body simulations and the evolution calculated by Eq. (32). Thus, we can conclude that the dispersion evolution of orbital eccentricities and inclinations of particles may be calculated using the equations derived in Section 2 together with the averaged rates which can be obtained using the numerical

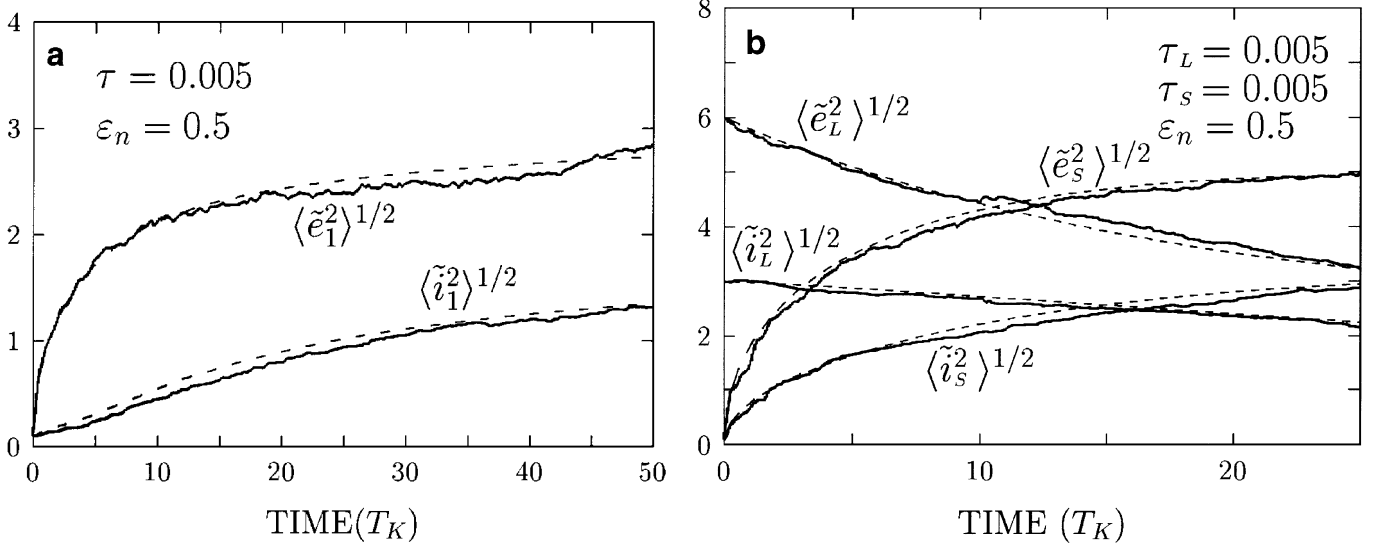


FIG. 10. Comparison between the evolution of root mean square eccentricity and inclination calculated by Eq. (32) (dashed lines) and numerical results of N -body simulations (solid lines). Time is given in units of the orbital period $T_K = 2\pi/\Omega$. (a) Case with a single size component. Initially, $\langle \tilde{e}_1^2 \rangle^{1/2} = \langle \tilde{i}_1^2 \rangle^{1/2} = 0.1$. (b) Case with two size components. Initially, $\langle \tilde{e}_L^2 \rangle^{1/2} = 6$, $\langle \tilde{i}_L^2 \rangle^{1/2} = 3$, and $\langle \tilde{e}_S^2 \rangle^{1/2} = \langle \tilde{i}_S^2 \rangle^{1/2} = 0.1$.

results of the three-body orbit integrations. In this case, dynamical evolution and equilibrium state can be investigated with less computational effort than direct N -body simulations; for example, evolutions with a number of various initial conditions can easily be examined once the 441 data points of the stirring rates are obtained using the numerical results of the three-body orbit integrations. We will discuss equilibrium velocity dispersions in the next section.

It should be noted that dynamical evolution of a disk of particles with large optical depth cannot be described by the above methods based on the results of three-body orbit integrations. In a system of large optical depth, collective effects should become important (Salo 1992b, 1995), which are not taken into account in the present formulation. However, it can be expected that the understanding of the low-optical-depth system based on the present formalism would also be useful in understanding the nature of characteristic dynamical behavior observed in a disk of large optical depth.

5. EQUILIBRIUM VELOCITY DISPERSIONS

In this section, we investigate equilibrium velocity dispersions of particles, using Eq. (32) together with the averaged stirring rates described in Section 4.2. The numerical procedures to find an equilibrium state are as follows. First, we give initial values of dispersions, such as $\langle \tilde{e}_1^2 \rangle$. Next, we calculate averaged stirring rates such as $\langle P_{VS} \rangle$, which are functions of dispersions of relative orbital elements $\langle \tilde{e}^2 \rangle$ and $\langle \tilde{i}^2 \rangle$, using Eqs. (12), (22), and (25) and the 441 data points obtained by the extrapolation of the numerical results of three-body orbit integrations (Section 4.2). Substituting these stirring rates into Eq. (32), the evolution of mean square eccentricities and inclinations is simulated. We repeat these calculations until an equilibrium state is

found or the dispersions go out of the range of $10^{-1} \leq \langle \tilde{e}_1^2 \rangle^{1/2}$ (or $\langle \tilde{i}_1^2 \rangle^{1/2} \leq 30$).

5.1. Case with a Single Size Component and Constant Coefficient of Restitution

First, we consider a system of particles with identical sizes. In this case, velocity evolution can be described only by viscous stirring rates $\langle P_{VS} \rangle$ and $\langle Q_{VS} \rangle$. Figure 11a was produced by using the numerical results of three-body orbit integrations with $\tilde{r}_p = 1$ and $\varepsilon_n = 0.5$. In this figure, thin arrows schematically indicate the direction and strength of the viscous stirring at each point on the $\langle \tilde{e}_1^2 \rangle^{1/2} - \langle \tilde{i}_1^2 \rangle^{1/2}$ plane. The angle between an arrow and the $\langle \tilde{e}_1^2 \rangle^{1/2}$ axis is given by $\theta = \tan^{-1}[(\langle Q_{VS} \rangle / \langle \tilde{i}_1^2 \rangle) / (\langle P_{VS} \rangle / \langle \tilde{e}_1^2 \rangle)]$, and its length is proportional to $\log[(\langle P_{VS} \rangle / \langle \tilde{e}_1^2 \rangle)^2 + (\langle Q_{VS} \rangle / \langle \tilde{i}_1^2 \rangle)^2 + 10^3]$, where 10^3 was added to define a lower limit to the arrow length so that the direction of evolution could be easily displayed even when the absolute value of the stirring rate is small. The thick line shows evolutionary paths which have been obtained by solving Eq. (32) numerically with three different initial conditions, $(\langle \tilde{e}_1^2 \rangle^{1/2}, \langle \tilde{i}_1^2 \rangle^{1/2}) = (0.1, 0.1)$, $(0.1, 10)$, and $(10, 0.1)$. It can be seen that the evolutionary path is nearly horizontal when $\langle \tilde{e}_1^2 \rangle^{1/2} \ll \langle \tilde{i}_1^2 \rangle^{1/2}$, while it is nearly vertical when $\langle \tilde{e}_1^2 \rangle^{1/2} \gg \langle \tilde{i}_1^2 \rangle^{1/2}$, in both cases heading for a state with $\langle \tilde{e}_1^2 \rangle^{1/2} \simeq \langle \tilde{i}_1^2 \rangle^{1/2}$. Moreover, viscous stirring of eccentricities is found to be much stronger than that of inclinations when $\langle \tilde{e}_1^2 \rangle^{1/2} \lesssim 2$, where Kepler shear dominates the relative velocity of particles. Thus, the evolutionary path is nearly horizontal in the low $\langle \tilde{e}_1^2 \rangle^{1/2}$ region even when $\langle \tilde{e}_1^2 \rangle^{1/2} > \langle \tilde{i}_1^2 \rangle^{1/2}$. We find that the same equilibrium state is achieved regardless of the choice of initial conditions; in the equilibrium state, $\langle \tilde{e}_1^2 \rangle^{1/2} \simeq 3.0$ and $\langle \tilde{i}_1^2 \rangle^{1/2} \simeq 1.7$.

For comparison, we have produced a similar figure using the analytic stirring rates calculated by Eq. (52) in Fig. 11b,

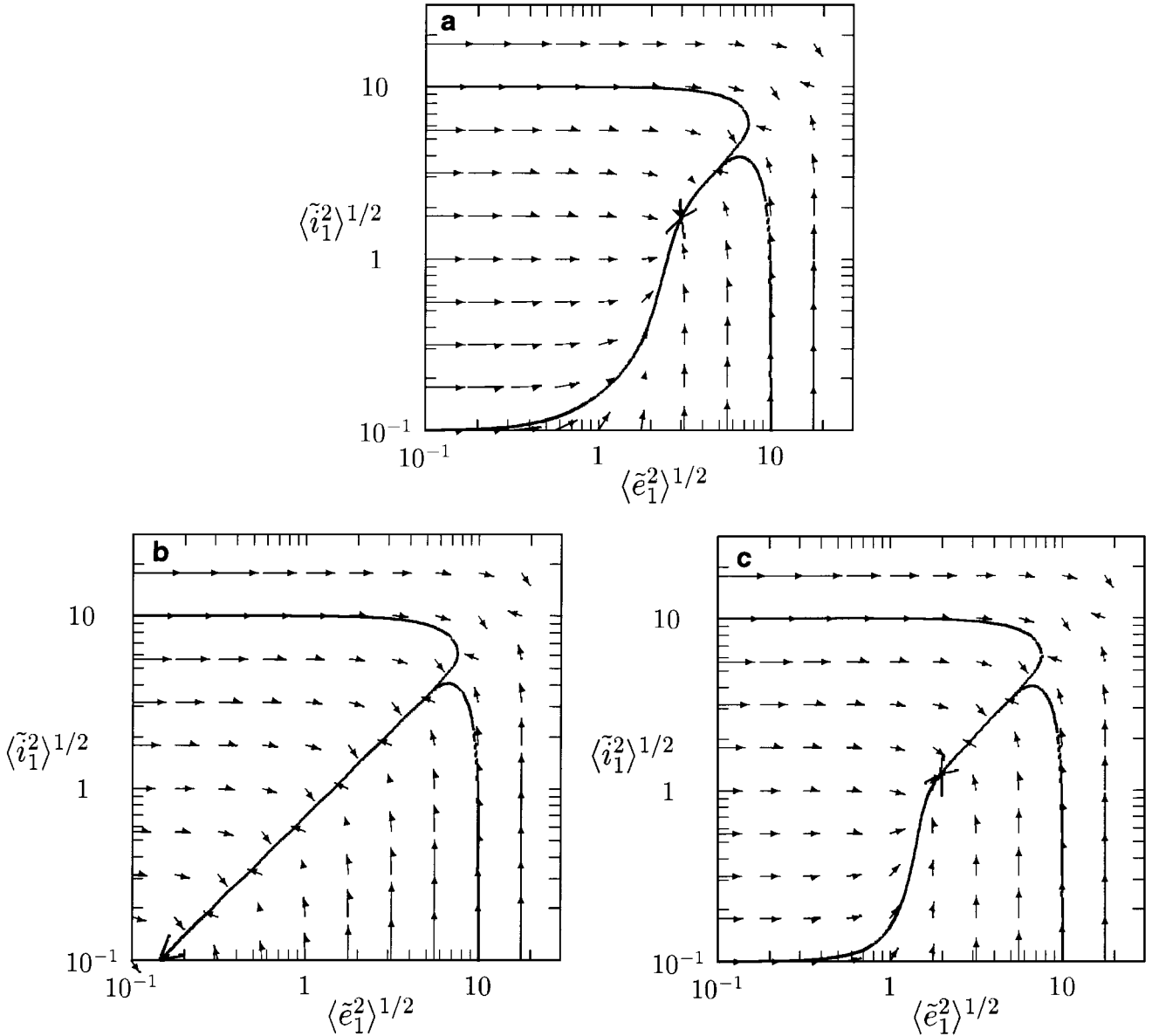


FIG. 11. (a) Thin arrows: directions of evolution schematically drawn using $\langle P_{VS} \rangle$ and $\langle Q_{VS} \rangle$ calculated from numerical results of three-body orbit integrations ($\tilde{r}_p = 1$ and $\varepsilon_n = 0.5$). Thick lines: evolutionary paths obtained by solving Eq. (32) numerically with three different initial conditions, $(\langle \tilde{i}_1^2 \rangle^{1/2}, \langle \tilde{e}_1^2 \rangle^{1/2}) = (0.1, 0.1)$, $(0.1, 10)$, and $(10, 0.1)$. (b) Same as (a), but the analytic stirring rates calculated by Eq. (52) are used. (c) Case for nongravitating particles with finite size; stirring rates obtained by orbit integrations with Eq. (63) are used.

and using the results of orbit integrations for nongravitating particles (see Eq. (63)) in Fig. 11c. In both cases, $\tilde{r}_p = 1$ and $\varepsilon_n = 0.5$. In the former case, the dispersions first evolve toward a state with $\langle \tilde{i}_1^2 \rangle^{1/2} / \langle \tilde{e}_1^2 \rangle^{1/2} \simeq 0.63$, and afterwards, both $\langle \tilde{e}_1^2 \rangle^{1/2}$ and $\langle \tilde{i}_1^2 \rangle^{1/2}$ decrease monotonically keeping the ratio constant. Since $\varepsilon_n (=0.5)$ is smaller than $\varepsilon_{\text{crit}}$ given by Eq. (60), no equilibrium state exists in this case. On the other hand, the evolutionary trend displayed in Fig. 11c is similar to that in Fig. 11a. An equilibrium state is also achieved in Fig. 11c, since the effect of finite size maintains a velocity dispersion at least comparable to $R_p \Omega$ (Brahic 1977). We find that $\langle \tilde{e}_1^2 \rangle^{1/2} \simeq 2.0$ and $\langle \tilde{i}_1^2 \rangle^{1/2} \simeq 1.2$ in the

equilibrium state, which are about 30% smaller than the values in the case with particle gravity.

Equilibrium velocity dispersions for different values of \tilde{r}_p are shown in Fig. 12 ($\varepsilon_n = 0.5$). We have carried out three-body orbit integrations with these values of \tilde{r}_p , and the stirring rates which were calculated in the manner described in Section 4.2 have been used to produce Fig. 12. It is found that the equilibrium values first decrease with increasing \tilde{r}_p , and then increase with increasing \tilde{r}_p when $\tilde{r}_p \gtrsim 1.4$. This behavior comes from the two effects controlling the equilibrium velocity dispersions: gravity and finite size. In Fig. 12, values of $\tilde{v}_e (= \sqrt{6/\tilde{r}_p})$ and \tilde{r}_p

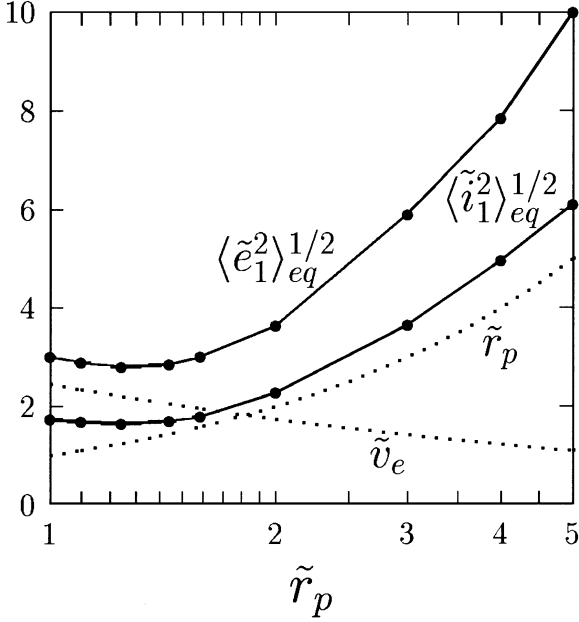


FIG. 12. Equilibrium values of $\langle \tilde{e}_1^2 \rangle^{1/2}$ and $\langle \tilde{i}_1^2 \rangle^{1/2}$ as a function of \tilde{r}_p ($\varepsilon_n = 0.5$). For comparison, values of $\tilde{v}_e (= \sqrt{6/\tilde{r}_p})$ and \tilde{r}_p are shown by the dotted lines.

are plotted by the dotted lines. We find that the behavior of the equilibrium values is similar to that of \tilde{v}_e when $\tilde{r}_p \lesssim 1.3$, while it is similar to that of \tilde{r}_p for larger values of \tilde{r}_p . Thus, it can be expected that equilibrium velocity dispersions should be of the order of \tilde{v}_e when $1 \lesssim \tilde{r}_p \lesssim 1.3$, while they should be of the order of \tilde{r}_p for larger values of \tilde{r}_p .

Figure 13 shows the cases of gravitating particles with four different values of ε_n ($\tilde{r}_p = 1$). When $\varepsilon_n = 0$ (Fig. 13a), the evolutionary trend is similar to the case of $\varepsilon_n = 0.5$, although the equilibrium values are slightly smaller. When ε_n is close to ε_{crit} ($\varepsilon_n = 0.63$; Fig. 13b), existence of an equilibrium state depends on the initial conditions; no equilibrium state exists unless initial values of both $\langle \tilde{e}_1^2 \rangle^{1/2}$ and $\langle \tilde{i}_1^2 \rangle^{1/2}$ are sufficiently small. We have found no equilibrium state when $\varepsilon_n \geq 0.64$; in this case, $\langle \tilde{e}_1^2 \rangle^{1/2}$ and $\langle \tilde{i}_1^2 \rangle^{1/2}$ first evolve toward a state of $\langle \tilde{i}_1^2 \rangle^{1/2} / \langle \tilde{e}_1^2 \rangle^{1/2} \simeq 0.63$ with $\langle \tilde{e}_1^2 \rangle^{1/2} \gtrsim 3$, and afterwards both of them increase monotonically (Figs. 13c and 13d, where the cases of $\varepsilon_n = 0.7$ and 1 are shown).

Figure 14 shows the plots of equilibrium values as a function of ε_n ; equilibrium values of $\langle \tilde{e}_1^2 \rangle^{1/2}$ and $\langle \tilde{i}_1^2 \rangle^{1/2}$ are shown in Fig. 14a, and those of $\beta = \langle \tilde{i}_1^2 \rangle^{1/2} / \langle \tilde{e}_1^2 \rangle^{1/2}$ are shown in Fig. 14b. For the cases with $\varepsilon_n = 0, 0.2$, and 0.5 , the equilibrium values for nongravitating finite size particles are also shown with star symbols. For example, we find $\langle \tilde{e}_1^2 \rangle_{eq}^{1/2} \simeq 2.7$ and $\langle \tilde{i}_1^2 \rangle_{eq}^{1/2} \simeq 1.2$ for gravitating particles when $\varepsilon_n = 0$. It can be seen in Fig. 14a that equilibrium velocity dispersions do not depend on ε_n significantly as long as $\varepsilon_n \lesssim 0.5$, while they increase with increasing ε_n when $\varepsilon_n > 0.5$. This can be attributed to the fact that stirring by gravitational scattering and finite size effects is more efficient than inelastic dissipation in such low velocity disper-

sion regions ($\langle \tilde{e}_1^2 \rangle^{1/2} \lesssim 2$). As a result, $\langle \tilde{e}_1^2 \rangle^{1/2}$ cannot become smaller than $\tilde{v}_e = \sqrt{6}$, regardless of the value of ε_n . It can be also found that we would substantially underestimate the equilibrium velocity dispersions if we neglected particle gravity. We find that the values of $\langle \tilde{e}_1^2 \rangle_{eq}^{1/2}$ of gravitating particles for $\varepsilon_n \simeq 0$ can be approximated by $\tilde{v}_e (= v_e / h v_K)$, while those of nongravitating particles can be approximated by $\tilde{r}_p (= 2 R_{p1} \Omega / h v_K)$. On the other hand, β_{eq} gradually increases with increasing ε_n , and its value becomes close to β_{crit} given by Eq. (60) as ε_n approaches ε_{crit} (Fig. 14b).

It is interesting to compare these figures with Fig. 11a of Salo (1995), which investigated the dependence of equilibrium velocity dispersions on ε_n in the case of relatively large optical depth ($\tau = 0.4$). Salo (1995) found that equilibrium horizontal velocity dispersions increase with decreasing ε_n when $\varepsilon_n < 0.6$, while our Fig. 14a demonstrates that they are nearly constant when $\varepsilon_n \lesssim 0.5$. Since our results based on Hill's approximations (or epicyclic approximations) correspond to the low-optical-depth limit of a particle disk, we can confirm the conclusion of Salo (1995) that the increase in the equilibrium horizontal velocity dispersions when $\varepsilon_n < 0.6$ is due to collective effects such as grouping of particles, which appear only in systems of large optical depth.

5.2. Case with Velocity-Dependent Coefficient of Restitution

So far, we have assumed that the restitution coefficient ε_n is constant. According to laboratory impact experiments with ice, ε_n decreases with increasing impact velocity. For example, Bridges *et al.* (1984) found that the impact velocity dependence of ε_n can be approximated as

$$\varepsilon_n(v_n) = \min \left\{ 0.32 \left(\frac{v_n}{v_0} \right)^{-0.234}, 1 \right\}, \quad (68)$$

where v_n is the normal component of impact velocity and $v_0 = 1 \text{ cm s}^{-1}$; this value of v_0 is denoted by $v_{0,B}$ in the subsequent discussion. The functional form of Eq. (68) with $v_0 = v_{0,B}$ is plotted in Fig. 15 by the solid line. The experiments of Bridges *et al.* (1984) were later improved by Hatzes *et al.* (1988); they carried out similar measurements at lower temperature with reduced amounts of frost in particle surfaces, and found considerably less inelastic behavior. Supulver *et al.* (1995) further performed an experiment to simulate glancing collisions and found that the energy loss for tangential motion was quite low. Recently, Higa *et al.* (1996, 1998) also performed measurements of $\varepsilon_n(v_n)$ with a wider range of impact velocities. They found that the average value of ε_n for a smooth ice ball is close to unity when the impact velocity is smaller than a certain critical value, at which fracture of the ball begins to occur and ε_n starts to decrease substantially. Although theoretical analyses of these experimental results have been also carried out (Dilley 1993, Higa *et al.* 1998), size and mass dependence of the restitution coefficient for realistic particles with rough surfaces has not yet been clarified.

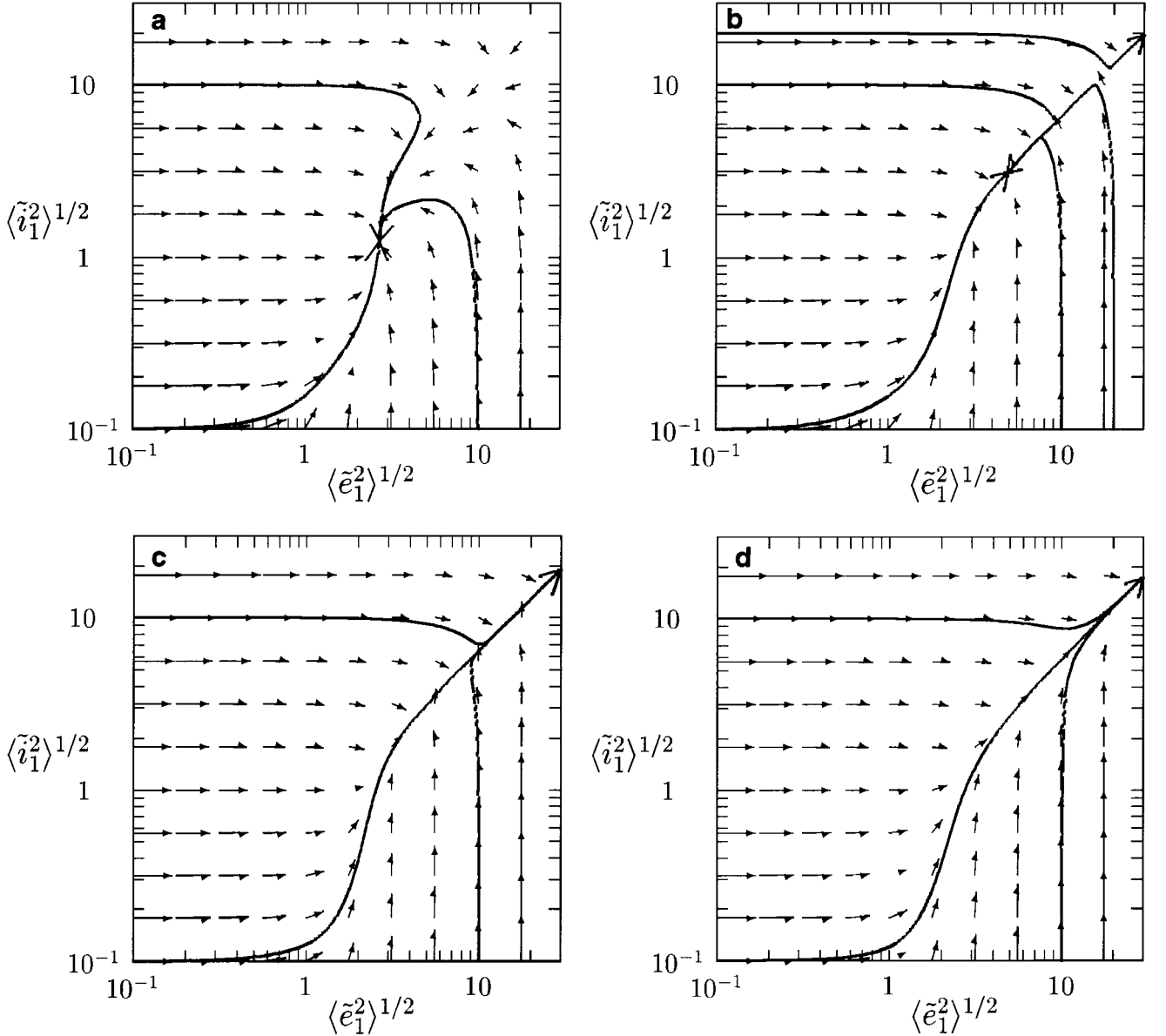


FIG. 13. Cases with four different values of ε_n ; (a) 0, (b) 0.63, (c) 0.7, and (d) 1. In the case of (b) where $\varepsilon_n = 0.63$, two additional evolutionary paths with the initial conditions of $(\langle \tilde{e}_1^2 \rangle^{1/2}, \langle \tilde{i}_1^2 \rangle^{1/2}) = (0.1, 20)$ and $(20, 0.1)$ are shown.

Here, as an example with a velocity-dependent coefficient of restitution, we apply the relation (68) to spherical particles with $R_p = 1$ m. Moreover, we assume that $M_c = 5.7 \times 10^{29}$ g, $a_0 = 1.22 \times 10^{10}$ cm, and $\rho_p = 0.9$ g cm $^{-3}$, so that $\tilde{r}_p = 1$ for collisions between particles of the same size (see Eq. (35)). In this case, $h = (2m/3M_c)^{1/3} = 1.64 \times 10^{-8}$. We integrate orbits by solving Eq. (5) as in the case of constant ε_n . At the time of impact, the normal component of relative velocity is calculated by $\tilde{v}_n = \tilde{\mathbf{x}} \cdot \tilde{\mathbf{x}}/\tilde{r}_p$. The unscaled value of the normal component of relative velocity can be calculated by

$$v_n = \tilde{v}_n h a_0 \Omega. \quad (69)$$

With Eqs. (68) and (69), the value of the restitution coefficient

for each impact can be obtained, and the components of rebound velocity are calculated with this coefficient. Using numerical results of three-body orbit integrations, we obtain stirring rates averaged over the Rayleigh distribution of eccentricities and inclinations in the manner described in Section 4.2. In the present case, however, we cannot evaluate the stirring rates with large \tilde{e} and \tilde{i} by extrapolation of numerical results, since the restitution coefficient depends on \tilde{e} and \tilde{i} through impact velocity. Thus, we calculate the stirring rates for $\tilde{e} > 10^{5/4}$ or $\tilde{i} > 10^{5/4}$ by semianalytical methods for nongravitating particles described in Sections 3.1 and 3.2 of Paper I (note that ξ and ξ_0 in Eqs. (3.14) and (3.16) of Paper I should read ζ and ζ_0 , respectively). Figure 16a was plotted using the stirring rates obtained with

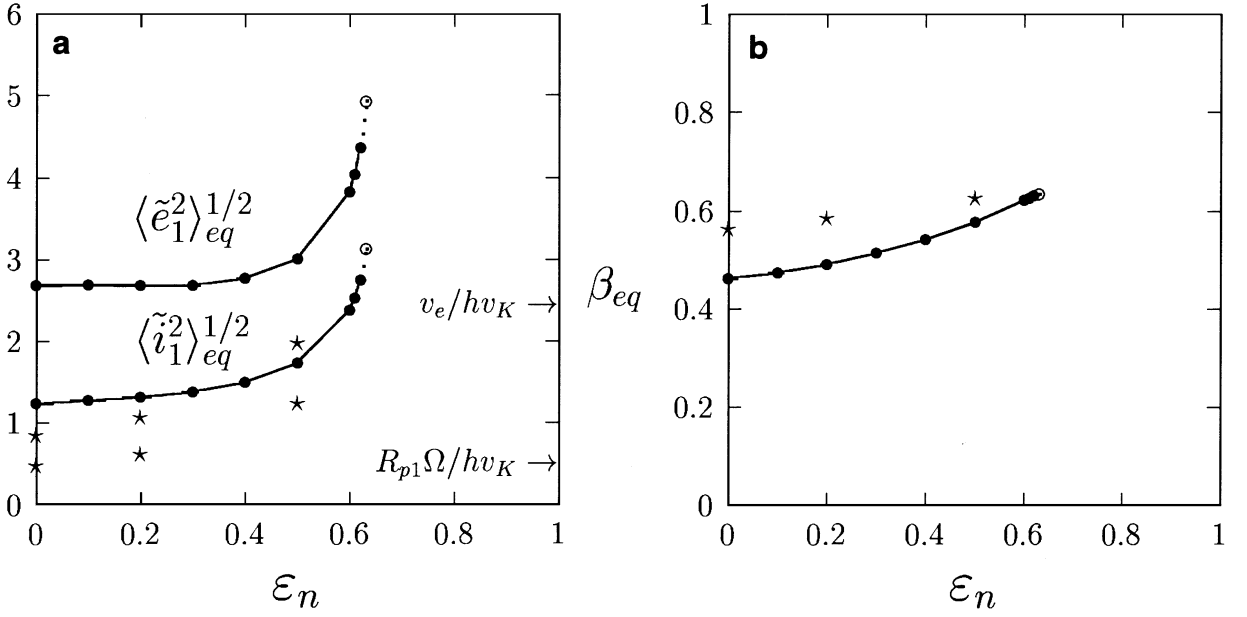


FIG. 14. (a) Equilibrium values of $\langle \tilde{e}_1^2 \rangle_{eq}^{1/2}$ and $\langle \tilde{i}_1^2 \rangle_{eq}^{1/2}$ for gravitating particles as a function of ϵ_n (lines with solid circles). Existence of an equilibrium state depends on the choice of initial conditions when $\epsilon_n = 0.63$ (open circles). No equilibrium state is found when $\epsilon_n \geq 0.64$. Those for nongravitating particles with finite size are also shown for comparison by the star symbols when $\epsilon_n = 0, 0.2$, and 0.5 . In all these cases, $\tilde{r}_p = 1$. The values of $R_{p1}\Omega$ (R_{p1} is the radius of a particle) and the escape velocity v_e scaled by $h v_K (= R_H \Omega)$ are also shown. (b) Equilibrium values of $\beta = \langle \tilde{i}_1^2 \rangle_{eq}^{1/2} / \langle \tilde{e}_1^2 \rangle_{eq}^{1/2}$ as a function of ϵ_n .

the above procedure. It can be seen that the general behavior is similar to the case of $\epsilon_n = 0.5$ (Fig. 11a) or $\epsilon_n = 0$ (Fig. 13a). This reflects the fact that the values of ϵ_n in most collisions in the present case are smaller than ϵ_{crit} unless scaled velocity dispersions are considerably smaller than unity (Fig. 15).

In order to study the effects of the functional form of $\epsilon_n(v_n)$ on equilibrium velocity dispersion, we examined three more cases with different values of v_0 , $v_0/v_{0,B} = 1/3, 3$, and 9 , where a larger value of $v_0/v_{0,B}$ corresponds to a more elastic case (Fig. 15). Figure 16b shows the plots of equilibrium values of the root mean square eccentricities and inclinations as a function of $v_0/v_{0,B}$. When $v_0/v_{0,B} = 3$ or 9 , it can be seen that equilibrium values are much larger than the case with $v_0/v_{0,B} = 1$, owing to more elastic properties of the particles. On the other hand, the equilibrium values in the case of $v_0/v_{0,B} = 1/3$ did not change substantially from those with $v_0/v_{0,B} = 1$. This is due to the effect of gravitational scattering of particles, which prevents $\langle \tilde{e}_1^2 \rangle_{eq}^{1/2}$ from becoming smaller than $\tilde{v}_e (= \sqrt{6})$, even when collisions are highly dissipative.

5.3. Case with a Bimodal Size Distribution

Finally, we investigate equilibrium velocity dispersions in a system consisting of two different sizes of particles. We assume that $\epsilon_n = 0.5$ and $m_L/m_S = 8$ and calculate velocity evolution using Eq. (32). Since masses of particles appear in Eq. (32) only in the form of a mass ratio, the values of m_L and m_S do not need to be specified. The values of M_c , a_0 , and ρ_p appearing in Eq. (35) are chosen so that $\tilde{r}_p = 1$ for collisions between m_L and m_S ; in this case, \tilde{r}_p for self-collisions (i.e., collisions between m_L

and m_L , or between m_S and m_S) is $(4/3)^{1/3} \simeq 1.1006$. We first calculate averaged stirring rates for $\tilde{r}_p = 1$ and 1.1006 using the numerical results of three-body orbit integrations. Substituting these rates into Eq. (32) and solving this equation for given

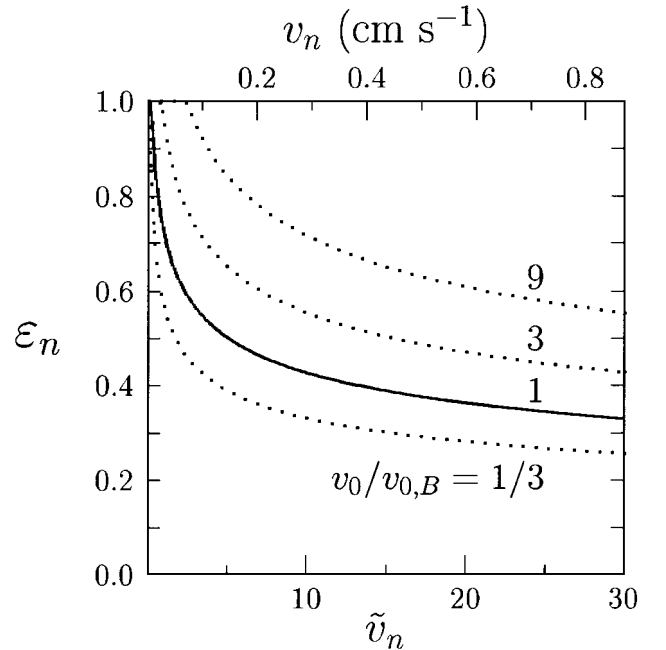


FIG. 15. Functional forms of velocity-dependent coefficient of restitution calculated by Eq. (68) with four different values of v_0 . The case of $v_0 = v_{0,B} (= 1 \text{ cm s}^{-1})$; solid line) corresponds to the experimental results of Bridges *et al.* (1984).

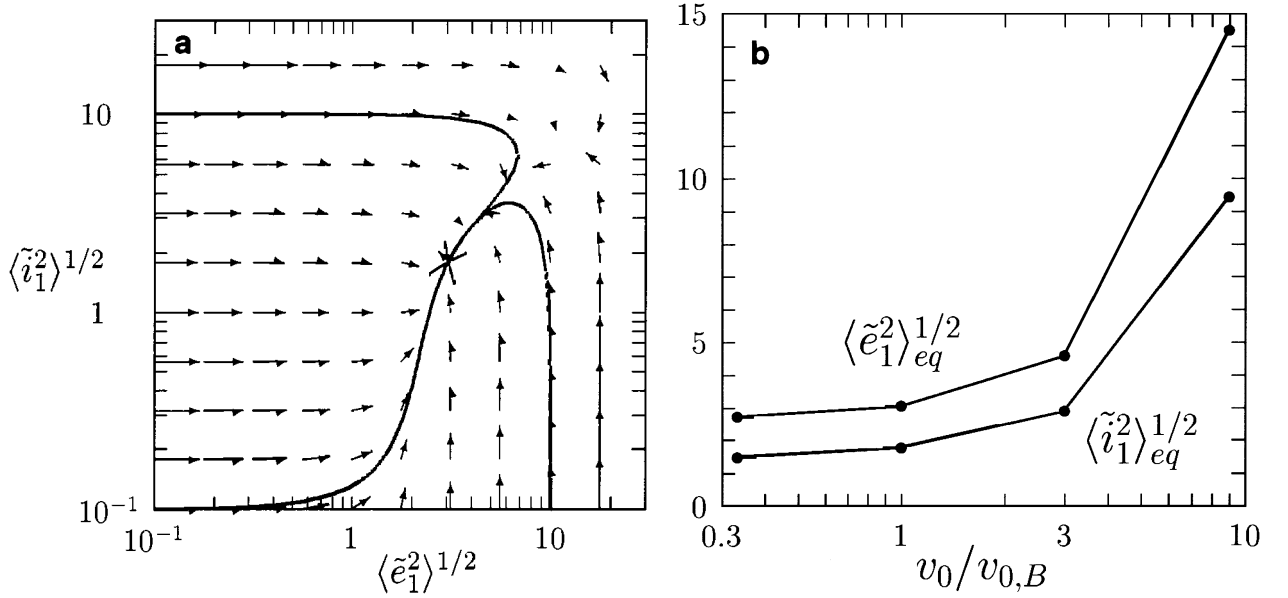


FIG. 16. (a) Same as Fig. 11a, but the velocity-dependent coefficient of restitution given by Eq. (68) with $v_0 = v_{0,B}$ is used. (b) Equilibrium values of $\langle \tilde{e}_1^2 \rangle^{1/2}$ and $\langle \tilde{i}_1^2 \rangle^{1/2}$ in the case with the velocity-dependent coefficient of restitution, as a function of $v_0/v_{0,B}$.

values of the surface number density of each component, we can calculate the velocity evolution and obtain equilibrium velocity dispersions, if any.

Figure 17 shows the equilibrium root-mean-squared eccentricity and inclination of each component as a function of the relative abundance of the two components (similar plots were obtained by Salo and Lukkari (1984), who performed N -body

simulations of planetary rings of nongravitating particles with a bimodal size distribution). Note that equilibrium values of $\langle \tilde{e}_L^2 \rangle^{1/2}$, etc., do not explicitly depend on τ_L or τ_S , but only on the ratio τ_L/τ_S . In Fig. 17, eccentricities and inclinations are normalized by $h_{LL} = (2m_L/3M_c)^{1/3}$, as in Fig. 10b. Figures 18a and 18b demonstrate the relative importance of the three terms of Eq. (32). For example, Eq. (32) for the evolution of $\langle \tilde{e}_L^2 \rangle$ can be written as

$$\frac{d\langle \tilde{e}_L^2 \rangle}{d\tilde{t}} = \Pi_{VS,LL} + \Pi_{VS,LS} + \Pi_{DF,LS}, \quad (70)$$

where

$$\begin{cases} \Pi_{VS,LL} = \frac{1}{4} \tilde{N}_{s,L} \tilde{h}_{LL}^4 \langle P_{VS} \rangle_{LL} \\ \Pi_{VS,LS} = \tilde{N}_{s,S} m_S'^2 \tilde{h}_{LS}^4 \langle P_{VS} \rangle_{LS} \\ \Pi_{DF,LS} = \tilde{N}_{s,S} m_S' \tilde{h}_{LS}^4 \frac{m_S' \langle \tilde{e}_S^2 \rangle - m_L' \langle \tilde{e}_L^2 \rangle}{\langle \tilde{e}_L^2 \rangle + \langle \tilde{e}_S^2 \rangle} \langle P_{DF} \rangle_{LS}. \end{cases} \quad (71)$$

Note that $\tilde{h}_{LL} = 1$ in the present case, since eccentricities and inclinations are normalized by h_{LL} . We similarly define the three terms describing the evolution of $\langle \tilde{e}_S^2 \rangle$ by $\Pi_{VS,SS}$, $\Pi_{VS,SL}$, and $\Pi_{DF,SL}$. The values of these three terms with $\tau_S = 0.005$ are shown in Figs. 18a and 18b. When they have negative values, they are shown by dashed curves.

When $\tau_L/\tau_S = 10^2$, it is found in Fig. 17 that $\langle \tilde{e}_L^2 \rangle^{1/2} = 2.88$ and $\langle \tilde{i}_L^2 \rangle^{1/2} = 1.68$. These values are quite close to those in the case of a single size component shown in Fig. 12, where we find $\langle \tilde{e}_1^2 \rangle^{1/2} = 2.89$ and $\langle \tilde{i}_1^2 \rangle^{1/2} = 1.69$ when $\tilde{r}_p = 1.1006$. The slightly smaller values of $\langle \tilde{e}_L^2 \rangle^{1/2}$ and $\langle \tilde{i}_L^2 \rangle^{1/2}$ in Fig. 17 are due to dynamical friction from small particles (Fig. 18a). On the other

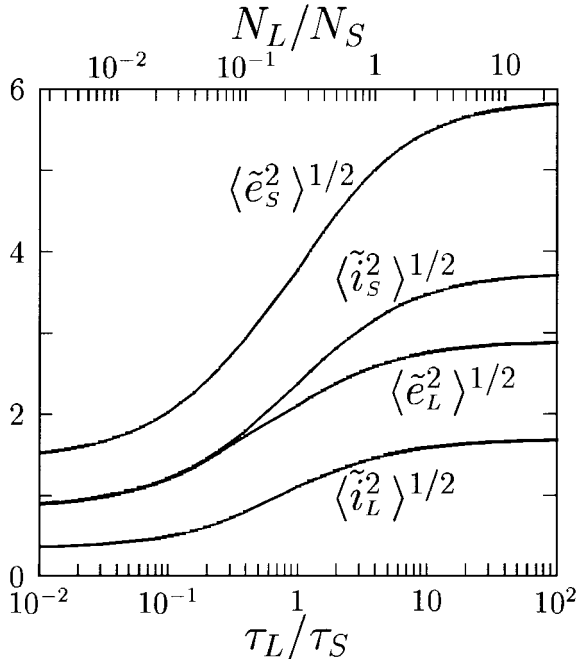


FIG. 17. Equilibrium values of root mean square eccentricities and inclinations of small and large particles as a function of their relative abundance.

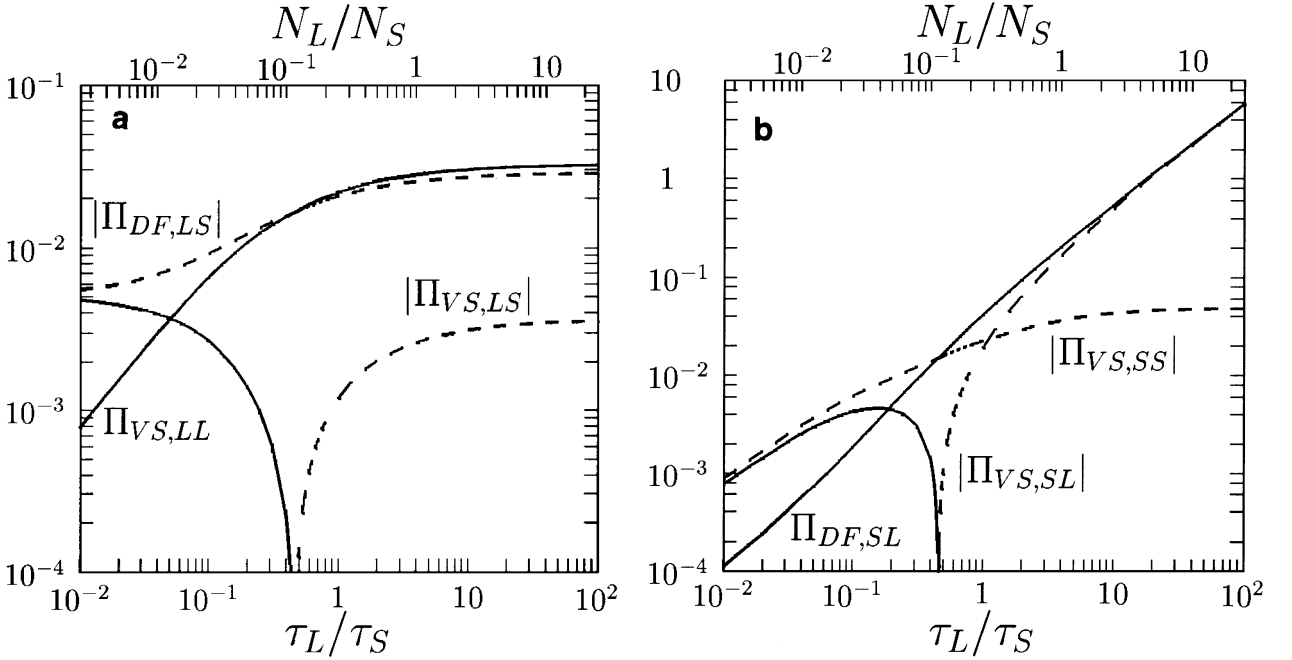


FIG. 18. (a) Values of three different terms in the evolution equation for $\langle \tilde{e}_S^2 \rangle$, as a function of relative abundance of the two size components. When they have negative values, their absolute values are shown by dashed lines. (b) Values of three different terms in the evolution equation for $\langle \tilde{e}_L^2 \rangle$.

hand, $\langle \tilde{e}_S^2 \rangle$ and $\langle \tilde{i}_S^2 \rangle$ in this case show much larger values than those of large particles, owing to energy input from large particles through the dynamical friction term (Fig. 18b). As we can confirm from Figs. 18a and 18b, the velocity of large particles in this case is determined mainly by the balance between viscous stirring between large particles and dynamical friction from small ones; the velocity of small particles in this case is determined by the balance between energy input from large particles through the dynamical friction term and inelastic dissipation in the viscous stirring term for collisions with large particles.

When $\tau_L/\tau_S = 10^{-2}$, on the other hand, it is found in Fig. 17 that $\langle \tilde{e}_S^2 \rangle^{1/2} = 1.52$ and $\langle \tilde{e}_L^2 \rangle^{1/2} = 0.89$; if we use $h_{SS} = (2m_S/3M_C)^{1/3}$ for scaling instead of h_{LL} , we have $\langle \tilde{e}_S^2 \rangle^{1/2} = 3.02$ and $\langle \tilde{i}_S^2 \rangle^{1/2} = 1.78$, which are close to but slightly larger than the values in a single component case, owing to the effect of viscous stirring caused by collisions with large particles (Fig. 18b). The velocity of large particles in this case is mainly determined by the balance between viscous stirring and dynamical friction by small particles (Fig. 18a).

Figures 18a and 18b show that $\Pi_{VS,LS}$ and $\Pi_{VS,SL}$ change their sign when $\tau_L/\tau_S \sim 0.5$. At this point, $\langle \tilde{e}_S^2 \rangle^{1/2} \sim 3$ and $\langle \tilde{e}_L^2 \rangle^{1/2} \sim 1.8$ (Fig. 17); if we use $h_{SL} = \{(m_S + m_L)/3M_C\}^{1/3}$ for scaling instead of h_{LL} , we have $\langle \tilde{e}^2 \rangle^{1/2} = (\langle \tilde{e}_S^2 \rangle + \langle \tilde{e}_L^2 \rangle)^{1/2} \sim 4$. It can be confirmed by Fig. 9 that $\langle P_{VS} \rangle_{SL}$ (and $\langle P_{VS} \rangle_{LS}$) with $\varepsilon_n = 0.5$ changing its sign around the above value of mean squared relative eccentricity.

Figure 19a shows the plots of $\beta_S = \langle \tilde{i}_S^2 \rangle^{1/2} / \langle \tilde{e}_S^2 \rangle^{1/2}$ and $\beta_L = \langle \tilde{i}_L^2 \rangle^{1/2} / \langle \tilde{e}_L^2 \rangle^{1/2}$ at equilibrium states. The value of β_S at $\tau_L/\tau_S = 10^{-2}$ and that of β_L at $\tau_L/\tau_S = 10^2$ are close to the value in a single size component case. The large value of β_S

at $\tau_L \gg \tau_S$ and the small value of β_L at $\tau_L \ll \tau_S$ reflect the effect of dynamical friction. In particular, the value of β_L ($\simeq 0.4$) when $\tau_L/\tau_S = 10^{-2}$ is much smaller than the case of a single size component. This is due to the small values of $\langle \tilde{e}_L^2 \rangle^{1/2}$ and $\langle \tilde{i}_L^2 \rangle^{1/2}$ caused by dynamical friction from small particles; in such low velocity regions ($\langle \tilde{e}_L^2 \rangle^{1/2} < 1$), viscous stirring of eccentricities is much stronger than that of inclinations (Section 4.1), thus β_L shows relatively small values. This can also be confirmed by Fig. 19b, which shows the plots of the ratios of random kinetic energy of large and small particles. We define the ratios of random kinetic energy of the two components in horizontal and vertical directions respectively as

$$\begin{cases} E_{r,L}/E_{r,S} = m_L \langle \tilde{e}_L^2 \rangle / m_S \langle \tilde{e}_S^2 \rangle \\ E_{z,L}/E_{z,S} = m_L \langle \tilde{i}_L^2 \rangle / m_S \langle \tilde{i}_S^2 \rangle. \end{cases} \quad (72)$$

In this figure, it can be seen that these ratios are bounded in a narrow range from 1.28 to 2.78 by the effect of dynamical friction, but they show deviation from complete equipartition of random kinetic energy (i.e., $E_{r,L}/E_{r,S} = 1$ and $E_{z,L}/E_{z,S} = 1$), owing to the effect of viscous stirring. The large values of $E_{r,L}/E_{r,S}$ and the small values of $E_{z,L}/E_{z,S}$ when $\tau_L/\tau_S \lesssim 10^{-1}$ can be attributed to efficient stirring of eccentricity of large particles in the low velocity region, as mentioned above.

6. CONCLUSIONS AND DISCUSSION

In the present work, we investigated the evolution of orbital eccentricities and inclinations of particles in a circumplanetary

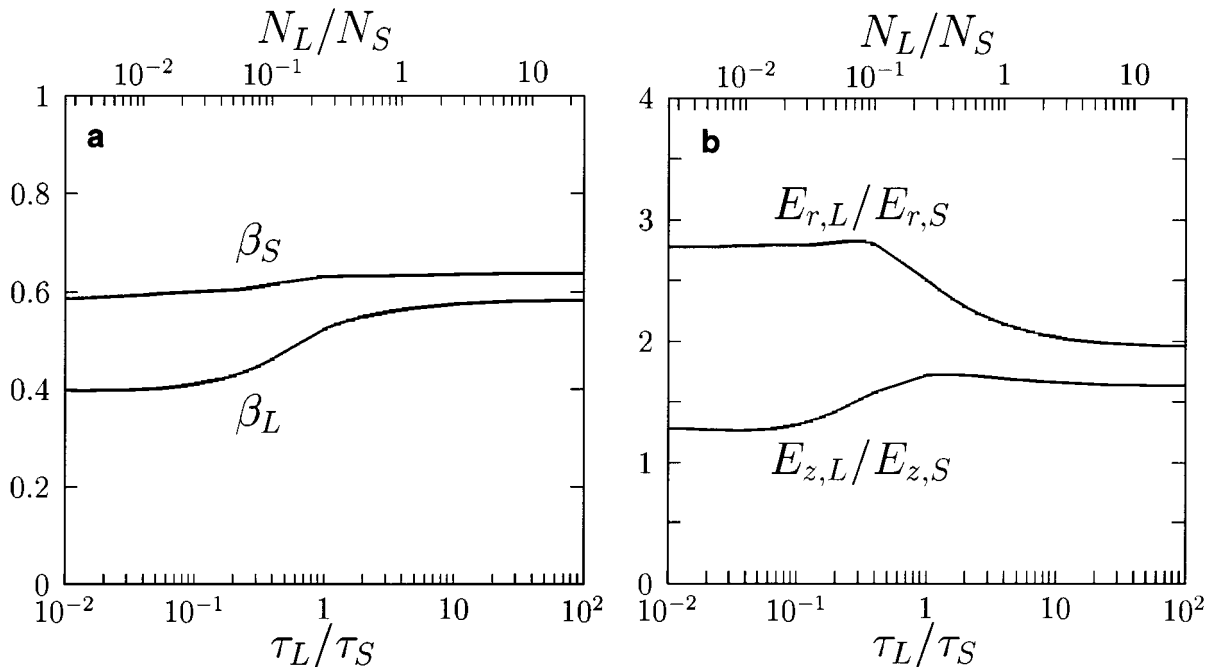


FIG. 19. (a) Equilibrium values of β of large and small particles as a function of their relative abundance. (b) The ratios of random kinetic energy of the two components defined by Eq. (72) as a function of their relative abundance.

disk, taking both direct collisions and gravitational interactions into account. In Section 2, we derived an evolution equation for the dispersions of eccentricities and inclinations of particles on the basis of the Hill's approximations in the three-body problem. We found that the evolution is governed by the terms of viscous stirring and energy equipartition, and the latter tends to equalize the product of mass and mean square eccentricities and inclinations of particles with different sizes. The evolution equation derived in Section 2 can also be applied to other particle disks with low optical thickness, such as a disk of planetesimals around the Sun. In Section 3, we analytically evaluated stirring rates of eccentricities and inclinations of nongravitating particles due to collisions. In the case where eccentricities and inclinations are assumed to be Rayleigh distributed, we confirmed that our results for the critical values of restitution coefficient and the ratio of root-mean-squared eccentricity and inclination coincide with the low-optical-depth limit of the results obtained by Goldreich and Tremaine (1978), who solved a Boltzmann equation for nongravitating ring particles with both low and high optical depths. In Section 4, we took into account the effect of gravitational interactions between particles, and the stirring rates were evaluated by three-body orbit integrations. Using numerically obtained stirring rates which were averaged over the Rayleigh distribution of eccentricities and inclinations, we simulated the evolution of the root-mean-squared eccentricities and inclinations of particles of one- and two-particle size components. Excellent agreement was found between these results based on three-body orbit integrations and those obtained by N -body simulations of systems with low optical depth. In Sec-

tion 5, we studied equilibrium velocity dispersions using the stirring rates obtained by the three-body orbit integrations. We confirmed that both finite size and gravity effects play an important role in maintaining nonzero velocity dispersions; the former effect retains the velocity dispersions to at least the order of $R_p\Omega$, while the latter prevents them from becoming smaller than the mutual escape velocity of particles.

As we mentioned in Section 5, the present results would be quite useful in the theoretical analyses of evolution and equilibrium states of particle velocity dispersions in a circumplanetary disk with low optical thickness. As an example, we clarified the relative importance of different terms appearing in the evolution equation for a system of two-particle size components (Fig. 18); this kind of analyses would be quite difficult in pure N -body simulations. Moreover, in numerical simulations of satellite accretion from small bodies using a coagulation equation, the evolution of velocity dispersions of particles with an arbitrary size distribution must be calculated correctly (Canup and Esposito 1995). Our present results can be extended so that they can be used in these numerical simulations. On the basis of the present formulation and numerical results, we will investigate the dynamical evolution of planetary rings and satellite accretion in future work. N -body simulations would be more useful in the study of the dynamical evolution of systems with large optical depths, to which our present analyses based on the Hill's approximations cannot be applied. We think that the combination of these two different approaches would be necessary in the understanding of dynamical behavior of planetary rings where the optical depth is close to unity.

APPENDIX A: STIRRING RATES IN THE HIGH VELOCITY LIMIT

In this appendix, we briefly describe procedures to obtain analytic expressions for the stirring rates (P_{VS} , Q_{VS} , P_{DF} , and Q_{DF}) due to inelastic collisions under the conditions (i) \tilde{e} , $\tilde{i} \gg \tilde{v}_e$ (i.e., mutual gravity can be neglected), (ii) \tilde{e} , $\tilde{i} \gg \tilde{r}_p$, and (iii) ε_n is constant. We analytically evaluated these stirring rates under the same conditions in Paper I, but errors in the numerical factors were introduced into the expression presented in that paper for the cases of $\tilde{i} \neq 0$ when the averages over impact positions were carried out (Eqs. (3.17) and (3.27) of Paper I).

The square of \tilde{e} and \tilde{i} can be expressed in terms of $\tilde{\mathbf{x}} = (\tilde{x}, \tilde{y}, \tilde{z})$ and $\dot{\tilde{\mathbf{x}}} = (\dot{\tilde{x}}, \dot{\tilde{y}}, \dot{\tilde{z}})$ as (Paper I)

$$\begin{aligned}\tilde{e}^2 &= (3\tilde{x} + \dot{\tilde{y}})^2 + \dot{\tilde{x}}^2 \\ \tilde{i}^2 &= \tilde{z}^2 + \dot{\tilde{z}}^2.\end{aligned}\quad (73)$$

The values of \tilde{e}^2 and \tilde{i}^2 immediately before the collision can be obtained by substituting the relative position at the time of impact for $\tilde{\mathbf{x}}$ and the impact velocity for $\dot{\tilde{\mathbf{x}}}$. If the velocity change is given by Eq. (43), the values of \tilde{e}^2 and \tilde{i}^2 immediately after the collision can also be calculated, and the changes in these quantities can be obtained as (Paper I)

$$\begin{aligned}\Delta\tilde{e}^2 &= \gamma\{4\tilde{y}(3\tilde{x} + \dot{\tilde{y}}) + 2\tilde{x}\dot{\tilde{x}} + \gamma(\tilde{x}^2 + 4\tilde{y}^2)\} \\ \Delta\tilde{i}^2 &= \gamma\tilde{z}(2\dot{\tilde{z}} + \gamma\tilde{z}),\end{aligned}\quad (74)$$

where

$$\gamma = -(1 + \varepsilon_n)(\tilde{\mathbf{x}} \cdot \dot{\tilde{\mathbf{x}}})/\tilde{r}_p^2. \quad (75)$$

For a given pair of \tilde{e} , \tilde{i} , and \tilde{b} , there exist four bands of collision orbits under the conditions (i) to (iii). The component of the relative velocity at $(\tilde{x}, \tilde{y}, \tilde{z}) = (0, 0, 0)$ in the unperturbed (neglecting mutual gravity) solution to Hill's equation is given by

$$(\dot{\tilde{x}}, \dot{\tilde{y}}, \dot{\tilde{z}}) = (\pm\sqrt{\tilde{e}^2 - \tilde{b}^2}, \tilde{b}/2, \pm\tilde{i}), \quad (76)$$

where each of four combinations of the signs of $\dot{\tilde{x}}$ and $\dot{\tilde{z}}$ respectively correspond to each of the four bands of collision orbits. We focus on one of these four bands with

$$(\dot{\tilde{x}}, \dot{\tilde{y}}, \dot{\tilde{z}}) = (-\sqrt{\tilde{e}^2 - \tilde{b}^2}, \tilde{b}/2, \tilde{i}), \quad (77)$$

since the total stirring rate can be obtained by simply multiplying the contribution of a single band by 4. In this case, under the conditions (i) to (iii), impact velocities for other collision orbits in the same band can be approximated by Eq. (77).

Furthermore, we introduce a new coordinate system $(\tilde{x}', \tilde{y}', \tilde{z}')$ defined by

$$\begin{pmatrix} \tilde{x} \\ \tilde{y} \\ \tilde{z} \end{pmatrix} = \begin{pmatrix} \sin\theta_0 & \cos\theta_0 & 0 \\ -\cos\theta_0 & \sin\theta_0 & 0 \\ 0 & 0 & 1 \end{pmatrix} \begin{pmatrix} \sin\theta_1 & 0 & \cos\theta_1 \\ 0 & 1 & 0 \\ -\cos\theta_1 & 0 & \sin\theta_1 \end{pmatrix} \begin{pmatrix} \tilde{x}' \\ \tilde{y}' \\ \tilde{z}' \end{pmatrix} \quad (78)$$

with

$$\begin{aligned}\cos\theta_0 &= \tilde{b} / \sqrt{\tilde{e}^2 - \frac{3}{4}\tilde{b}^2} \\ \sin\theta_0 &= \sqrt{\tilde{e}^2 - \tilde{b}^2} / \sqrt{\tilde{e}^2 - \frac{3}{4}\tilde{b}^2} \\ \cos\theta_1 &= i / \sqrt{\tilde{e}^2 + \tilde{i}^2 - \frac{3}{4}\tilde{b}^2} \\ \sin\theta_1 &= \sqrt{\tilde{e}^2 - \frac{3}{4}\tilde{b}^2} / \sqrt{\tilde{e}^2 + \tilde{i}^2 - \frac{3}{4}\tilde{b}^2}\end{aligned}\quad (79)$$

Using Eqs. (74), (75), and (77) to (79), $\Delta\tilde{e}^2$ and $\Delta\tilde{i}^2$ can be expressed in terms of \tilde{e} , \tilde{i} , \tilde{b} , and $\tilde{\mathbf{x}}'$, where $\tilde{\mathbf{x}}'$ is the relative position at the time of impact in the new coordinate system. By taking averages of $\Delta\tilde{e}^2$ and $\Delta\tilde{i}^2$ over \tilde{y}' and \tilde{z}' , we obtain the average contribution from the band with the impact velocity given by Eq. (77). On the other hand, the collision probability and Kepler shear velocity for given \tilde{e} , \tilde{i} , and \tilde{b} is expressed as $(2\tilde{r}_p/3\pi\tilde{b}\tilde{i}) \times \sqrt{(\tilde{e}^2 + \tilde{i}^2 - \frac{3}{4}\tilde{b}^2)/(\tilde{e}^2 - \tilde{b}^2)}$ and $\frac{3}{2}\tilde{b}$, respectively (Nakazawa *et al.* 1989). Multiplying these quantities by $\Delta\tilde{e}^2$ (or $\Delta\tilde{i}^2$) and integrating over \tilde{b} , we finally obtain P_{VS} (or Q_{VS}), which is given by Eq. (45).

P_{DF} and Q_{DF} in Eq. (45) can be obtained in a similar manner using $\Delta\tilde{e}_{||}$ and $\Delta\tilde{i}_{||}$ given by

$$\begin{aligned}\Delta\tilde{e}_{||} &= \gamma(6\tilde{x}\tilde{y} + \tilde{x}\dot{\tilde{x}} + 4\tilde{y}\dot{\tilde{y}})/\tilde{e} \\ \Delta\tilde{i}_{||} &= \gamma\tilde{z}\dot{\tilde{z}}/\tilde{i}.\end{aligned}\quad (80)$$

APPENDIX B: STIRRING RATES IN THE HIGH VELOCITY LIMIT WITH VELOCITY DISTRIBUTION

In this appendix, we describe procedures to obtain analytic expressions of the stirring rates due to inelastic collisions for the case with a Rayleigh distributions of eccentricities and inclinations. We adopt the same variable transformations described by Greenzweig and Lissauer (1992), who analytically obtained the accretion rate of a protoplanet embedded in a swarm of planetesimals with a Rayleigh distributions of eccentricities and inclinations.

The stirring rates in the high velocity limit averaged over the Rayleigh distribution are obtained by substituting Eqs. (45)

into Eqs. (25). In order to evaluate the integrals appearing in Eqs. (25), we need to obtain the Rayleigh distribution averages of $E(k)\tilde{e}^2\sqrt{1+(\tilde{e}/\tilde{i})^2}$, $E(k)\tilde{i}^2\sqrt{1+(\tilde{e}/\tilde{i})^2}$, and $F(k)\tilde{e}^2\sqrt{1+(\tilde{e}/\tilde{i})^2}$ (k is given by Eq. (46)). Following Greenzweig and Lissauer (1992), we define new coordinates u and ψ as

$$\begin{aligned} u &= \tilde{e}^2 + \tilde{i}^2, \\ \psi &= \tan^{-1}(\tilde{i}/\tilde{e}). \end{aligned} \quad (81)$$

For example, the Rayleigh distribution average of $E(k)\tilde{e}^2\sqrt{1+(\tilde{e}/\tilde{i})^2}$ can be written in terms of these variables as

$$\begin{aligned} &\langle E(k)\tilde{e}^2\sqrt{1+(\tilde{e}/\tilde{i})^2} \rangle \\ &= \int_0^\infty \int_0^\infty \frac{4\tilde{e}^3\tilde{i}E(k)}{\langle \tilde{e}^2 \rangle \langle \tilde{i}^2 \rangle} \sqrt{1+(\tilde{e}/\tilde{i})^2} \\ &\quad \times \exp\left\{-\frac{\tilde{e}^2}{\langle \tilde{e}^2 \rangle} - \frac{\tilde{i}^2}{\langle \tilde{i}^2 \rangle}\right\} d\tilde{e} d\tilde{i} \\ &= \frac{2}{\langle \tilde{e}^2 \rangle \langle \tilde{i}^2 \rangle} \int_0^{\pi/2} d\psi E\left(\frac{\sqrt{3}}{2} \cos \psi\right) \cos^3 \psi \\ &\quad \times \int_0^\infty du u^2 \exp\left\{-u\left(\frac{\cos^2 \psi}{\langle \tilde{e}^2 \rangle} + \frac{\sin^2 \psi}{\langle \tilde{i}^2 \rangle}\right)\right\}. \end{aligned} \quad (82)$$

Performing the integral over u , and making the substitution $\chi = \sin \psi$ and $\beta = \langle \tilde{i}^2 \rangle^{1/2} / \langle \tilde{e}^2 \rangle^{1/2}$, we get

$$\langle E(k)\tilde{e}^2\sqrt{1+(\tilde{e}/\tilde{i})^2} \rangle = 4\langle \tilde{e}^2 \rangle^{1/2} \langle \tilde{i}^2 \rangle^{1/2} I_e(\beta), \quad (83)$$

where $I_e(\beta)$ is defined by Eq. (54). In the same manner, the Rayleigh distribution averages of $E(k)\tilde{i}^2\sqrt{1+(\tilde{e}/\tilde{i})^2}$ and $F(k)\tilde{e}^2\sqrt{1+(\tilde{e}/\tilde{i})^2}$ can also be obtained as

$$\begin{cases} \langle E(k)\tilde{i}^2\sqrt{1+(\tilde{e}/\tilde{i})^2} \rangle = 4\langle \tilde{e}^2 \rangle^{1/2} \langle \tilde{i}^2 \rangle^{1/2} I_i(\beta) \\ \langle F(k)\tilde{e}^2\sqrt{1+(\tilde{e}/\tilde{i})^2} \rangle = 4\langle \tilde{e}^2 \rangle^{1/2} \langle \tilde{i}^2 \rangle^{1/2} J_e(\beta), \end{cases} \quad (84)$$

where $I_i(\beta)$ and $J_e(\beta)$ are given by Eq. (54). Using these quantities, we finally obtain Eq. (52).

ACKNOWLEDGMENTS

I am grateful to Hidekazu Tanaka, Shigeru Ida, and Sei-ichiro Watanabe for helpful comments, and Doug Sawyer for improving the English of the manuscript. I also thank Derek Richardson for thoughtful review of the manuscript and useful advice on the English writing, and Heikki Salo for providing useful comments and carrying out his own simulation to confirm the results of the present work. This work was supported by the Grant-in-Aid of the Japanese Ministry of Education, Science, Sports, and Culture (09440089), and by the Center for Planning and Information Systems of the Institute of Space and Astronautical Science.

REFERENCES

- Araki, S., and S. Tremaine 1986. The dynamics of dense particle disks. *Icarus* **65**, 83–109.
- Brahic, A. 1977. Systems of colliding bodies in a gravitational field: Numerical simulation of the standard model. *Astron. Astrophys.* **54**, 895–907.
- Bridges, F., A. P. Hatzes, and D. N. C. Lin 1984. Structure, stability, and evolution of Saturn's rings. *Nature* **309**, 333–335.
- Brophy, T. G., G. R. Stewart, and L. W. Esposito 1990. A phase-space fluid simulation of a two-component narrow planetary ring: Particle size segregation, edge formation, and spreading rates. *Icarus* **83**, 133–155.
- Canup, R. M., and L. W. Esposito 1995. Accretion in the Roche zone: Coexistence of rings and ringmoons. *Icarus* **113**, 331–352.
- Canup, R. M., and L. W. Esposito 1996. Accretion of the Moon from an impact-generated disk. *Icarus* **119**, 427–446.
- Dilley, J. P. 1993. Energy loss in collisions of icy spheres: Loss mechanism and size-mass dependence. *Icarus* **105**, 225–234.
- Dones, L., and S. Tremaine 1993. On the origin of planetary spins. *Icarus* **103**, 67–92.
- Esposito, L. W. 1993. Understanding planetary rings. *Ann. Rev. Earth Planet. Sci.* **21**, 487–523.
- Goldreich, P., and S. Tremaine 1978. The velocity dispersion in Saturn's rings. *Icarus* **34**, 227–239.
- Goldreich, P., and S. Tremaine 1982. The dynamics of planetary rings. *Ann. Rev. Astron. Astrophys.* **20**, 249–283.
- Greenzweig, Y. and J. J. Lissauer 1990. Accretion rates of protoplanets. *Icarus* **87**, 40–77.
- Greenzweig, Y. and J. J. Lissauer 1992. Accretion rates of protoplanets. II. Gaussian distribution of planetesimal velocities. *Icarus* **100**, 440–463.
- Hatzes, A. P., F. Bridges, and D. N. C. Lin 1988. Collisional properties of ice spheres at low impact velocities. *Mon. Not. R. Astron. Soc.* **213**, 1091–1115.
- Hénon, M., and J.-M. Petit 1986. Series expansions for encounter-type solutions of Hill's problem. *Celest. Mech.* **38**, 67–100.
- Higa, M., M. Arakawa, and N. Maeno 1996. Measurements of restitution coefficients of ice at low temperatures. *Planet. Space Sci.* **44**, 917–925.
- Higa, M., M. Arakawa, and N. Maeno 1998. Size dependence of restitution coefficients of ice in relation to collision strength. *Icarus* **133**, 310–320.
- Hill, G. W. 1878. Researches in the lunar theory. *Am. J. Math.* **1**, 5–26, 129–147, 245–260.
- Hornung, P., R. Pellat, and P. Barge 1985. Thermal velocity equilibrium in the protoplanetary cloud. *Icarus* **64**, 295–307.
- Ida, S. 1990. Stirring and dynamical friction rates of planetesimals in the solar gravitational field. *Icarus* **88**, 129–145.
- Ida, S., and J. Makino 1992. N -body simulation of gravitational interaction between planetesimals and a planet. I. Velocity distribution of planetesimals. *Icarus* **96**, 107–120.
- Ida, S., R. M. Canup, and G. R. Stewart 1997. Lunar accretion from an impact-generated disk. *Nature* **389**, 353–357.
- Lissauer, J. J., and G. R. Stewart 1993. Growth of planets from planetesimals. In *Protostars & Planets III* (E. H. Levy and J. I. Lunine, Eds.), pp. 1061–1088. Univ of Arizona Press, Tucson.
- Lukkari, J., and H. Salo 1984. Numerical simulations of collisions in self-gravitating systems. *Earth Moon Planets* **31**, 1–13.
- Nakazawa, K., and S. Ida 1988. Hill's approximation in the three-body problems. *Prog. Theor. Phys. Suppl.* **96**, 167–174.
- Nakazawa, K., S. Ida, and Y. Nakagawa 1989. Collisional probability of planetesimals revolving in the solar gravitational field. I. Basic formulation. *Astron. Astrophys.* **220**, 293–300.
- Nicholson, P. D., and L. Dones 1991. Planetary rings. *Rev. Geophys.* **29**, 313–327.

- Ohtsuki, K. 1992a. Equilibrium velocities in planetary rings with low optical depth. *Icarus* **95**, 265–282. [Paper I]
- Ohtsuki, K. 1992b. Evolution of random velocities of planetesimals in the course of accretion. *Icarus* **98**, 20–27.
- Ohtsuki, K. 1993. Capture probability of colliding planetesimals: Dynamical constraints on accretion of planets, satellites, and ring particles. *Icarus* **106**, 228–246.
- Ohtsuki, K., and S. Ida 1990. Runaway planetary growth with collision rate in the solar gravitational field. *Icarus* **85**, 499–511.
- Ohtsuki, K., S. Ida, Y. Nakagawa, and K. Nakazawa 1993. Planetary accretion in the solar gravitational field. In *Protostars & Planets III* (E. H. Levy and J. I. Lunine, Eds.), pp. 1089–1107. Univ. of Arizona Press, Tucson.
- Petit, J.-M., and M. Hénon 1986. Satellite encounters. *Icarus* **66**, 536–555.
- Petit, J.-M., and M. Hénon 1987. A numerical simulation of planetary rings. I. Binary encounters. *Astron. Astrophys.* **173**, 389–404.
- Richardson, D. C. 1994. Tree code simulations of planetary rings. *Mon. Not. R. Astron. Soc.* **269**, 493–511.
- Salo, H. 1985. Numerical simulations of collisions and gravitational encounters in systems of non-identical particles. *Earth, Moon, Planets* **33**, 189–200.
- Salo, H. 1991. Numerical simulations of dense collisional systems. *Icarus* **90**, 254–270.
- Salo, H. 1992a. Numerical simulations of dense collisional systems. II. Extended distribution of particle sizes. *Icarus* **96**, 85–106.
- Salo, H. 1992b. Gravitational wakes in Saturn's rings. *Nature* **359**, 619–621.
- Salo, H. 1995. Simulations of dense planetary rings. III. Self-gravitating identical particles. *Icarus* **117**, 287–312.
- Salo, H., and J. Lukkari 1984. Numerical simulations of collisions in systems of non-identical particles. *Earth Moon Planets* **30**, 229–243.
- Stevenson, D. J., A. W. Harris, and J. I. Lunine 1984. Origin of satellites. In *Satellites* (J. A. Burns and M. S. Matthews, Eds.), pp. 39–88. Univ of Arizona Press, Tucson.
- Stewart, G. R., and S. Ida 1998. Velocity evolution of planetesimals: Unified analytical formulae and comparisons with *N*-body simulations. *Icarus*, submitted.
- Stewart, G. R., and G. W. Wetherill 1988. Evolution of planetesimal velocities. *Icarus* **74**, 542–553.
- Supulver, K. D., F. G. Bridges, and D. N. C. Lin 1995. The coefficient of restitution of ice particles in glancing collisions: Experimental results for unfrosted surfaces. *Icarus* **113**, 188–199.
- Trulsen, J. 1972. Numerical simulation of jetstreams. *Astrophys. Space Sci.* **17**, 241–262.
- Weidenschilling, S. J., C. R. Chapman, D. R. Davis, and R. Greenberg 1984. Ring particles: Collisional interactions and physical nature. In *Planetary Rings* (R. Greenberg and A. Brahic, Eds.), pp. 367–415. Univ. of Arizona Press, Tucson.
- Wisdom, J., and S. Tremaine 1988. Local simulations of planetary rings. *Astron. J.* **95**, 925–940.